Reprinted from *Printed in U.S.A.*

THE PHYSICS OF FLUIDS VOLUME 13, NUMBER 5 MAY 1970

Convective Losses in a Thermionic Plasma with Shear

DAVID MOSHER* AND FRANCIS F. CHEN
Plasma Physics Laboratory, Princeton University, Princeton, New Jersey
(Received 6 May 1969; final manuscript received 3 November 1969)

Experiments on anomalous transport in a Q machine with a hard core providing magnetic shear show shear-dependent particle losses in the absence of oscillations. It is demonstrated that these Bohm-like losses are caused by steady plasma convection in asymmetric electric fields produced by small temperature gradients in the end plates and that the effect of shear is to symmetrize the convective patterns by twisting the equipotentials into tight spirals. A finite-Larmor-radius theory of transport by convection is presented which correctly predicts the observed increase of confinement with shear. Estimates of the absolute magnitude of losses by this mechanism indicate that at least half of the anomalous transport in Q machines is due to plasma convection, at least in magnetic fields below 4 kG.

I. INTRODUCTION

A. Historical Background

Thermally ionized alkali-metal plasmas in Q machines[1] provide an ideal medium in which to study anomalous plasma transport across magnetic fields because the amplitude of low-frequency oscillations can be controlled by the experimenter. Universal instabilities can be suppressed by line tying at the end plates,[2] ion–ion collisions,[3] or nonuniform radial electric fields.[4] In this work we make use of stabilization by magnetic shear.[5]

In spite of the fact that anomalous transport in Q machines has been under scrutiny for nearly a decade, it is only now that an understanding of the basic physical phenomena is beginning to emerge. Early work by D'Angelo and Rynn[6] purported to show classical diffusion and recombination, albeit with a large coefficient of recombination later explained by von Goeler[7] as being due to surface recombination on the hot end plates. In these early experiments, the rate of diffusion was deduced from the spreading of the plasma profile. More recent experiments by Motley and von Goeler[8] and by Hashmi *et al.*,[9] however, have shown that this method is an insensitive one for distinguishing between classical and anomalous diffusion. A better method, used by D'Angelo[10] and Motley,[11] rests on the plot of plasma density n vs the flux Φ of ions injected at the end plates by surface ionization of neutral atoms. It can be shown that on such a plot one has $n \propto \Phi^{1/2}$ if classical diffusion and end-plate recombination are dominant, whereas $n \propto \Phi$ if a density-independent loss rate, such as Bohm diffusion,[12] obtains. What is generally found is that at high densities or low plate temperatures T_e, when the classical loss rate is large, the $n \propto \Phi^{1/2}$ law is followed, but that at low densities and high plate temperatures the $n \propto \Phi$ law is followed and the equilibrium density falls well below the classical value, indicating the existence of an anomalous loss process. At $T_e = 2400°K$, the transition point occurs at $n \approx 2 \times 10^{11}$ cm^{-3}. An example of an n-Φ plot, taken from our own data, is shown in Fig. 1. It covers only the low-density regime and clearly shows $n \propto \Phi$. The existence of an anomalous loss at low densities has been confirmed by von Goeler and Motley[13] using an entirely different technique: the atomic beam is interrupted, and the plasma decay time is directly measured. A suggestion by D'Angelo and von Goeler[14] that recombination on the probes can be a serious loss mechanism does

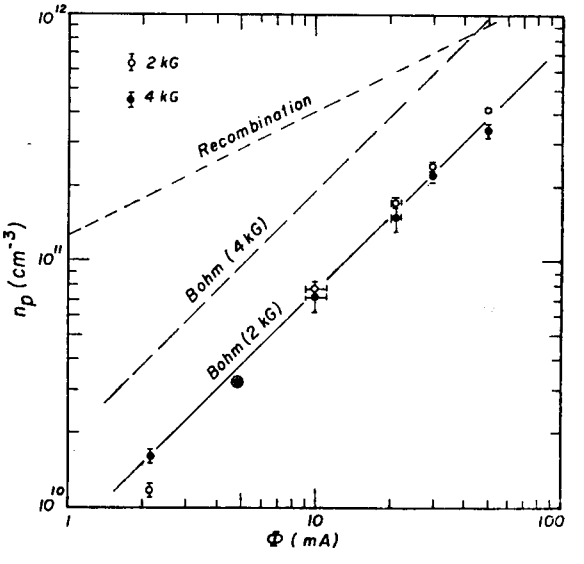

FIG. 1. Plot of peak density n_p vs input ion flux Φ at $B = 2$ and 4 kG. The data were taken in a 5.08-cm-diam K plasma 326 cm long with a plain W hot plate (no hard core) at 2500°K at each end. The neutral flux was concentrated at the center of the hot plates and was balanced to better than ±3% at the two ends. The straight lines are estimates of the density expected from classical processes (in this case, mainly end-plate recombination) and from Bohm diffusion. In this run, the points show no B dependence because it happens to be canceled out by a change in oscillation amplitude with B.

not invalidate the low-density conclusions, as has been shown by density measurements with microwaves.[13,15]

Supplementing the foregoing experiments are a number of direct measurements of the radial escape flux. Using a radial particle collector, Buchel'nikova[16] reported anomalous losses at low densities. Working with single-ended Q machines (a hot plate at one end and a cold collector at the other) Wolf and Rogers[17] and Decker *et al.*[18] used similar methods to measure the radial losses: an ion collector is moved progressively farther from the hot plate, and the decrease in collected flux is attributed to radial losses. The results were divergent: Wolf and Rogers reported essentially classical diffusion, while Decker *et al.* found $D_\perp > D_{\text{Bohm}}$. Eastlund *et al.*[19,20] used still another method: a pulse of neutral atoms is injected at the hot plate, and the radial and longitudinal spreading of the resulting pulse of ions is measured. The radial diffusion was found to be negligible in one paper,[19] and to be four orders of magnitude larger than classical in another paper.[20] Thus, no general conclusion can be drawn from these experiments on gross loss rates, experiments in which one does not examine what is happening inside the plasma.

A correlation between oscillations and diffusion has been reported by Buchel'nikova[15] and by Josephy *et al.*[21] These results are suspect, however, because either the observed oscillation amplitude[16] or the observed change in oscillation amplitude[21] is too small to explain the measured $D_\perp$ or change in $D_\perp$. Decker *et al.*[18] reported a total lack of correlation between oscillations and losses when a minimum-B field was applied to the plasma. On the other hand, Hendel *et al.*[22] have found a definite correlation between the onset of drift waves and a spreading of the plasma profile. In this experiment, however, the absolute loss rate was not measured, so that it could be consistent with the result of Decker *et al.*[18] if the dominant loss process were other than drift waves.

B. Evidence for Convection

In the present experiment, we can separate the steady-state losses from those connected with oscillations by suppressing the oscillations with a small amount of shear. Figure 2 shows our previously published data[23] on the decrease of $D_\perp$ with increasing shear. From the observed decrease in oscillation amplitude with shear, we conjectured at that time that the stabilization and localization of drift waves were responsible for the improved confinement. It

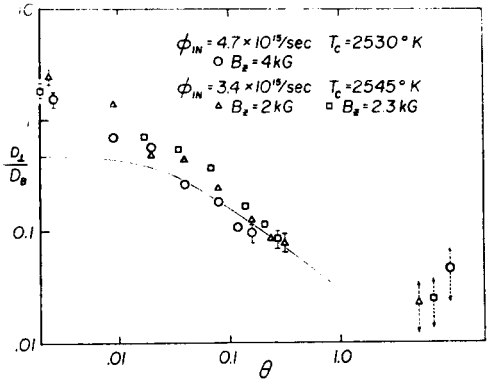

FIG. 2. Dependence of measured diffusion coefficient $D_\perp$ (normalized to the Bohm coefficient D_B) on shear parameter θ. The points at extreme right are estimates of classical losses (from Ref. 23).

now appears that only the losses occurring at low values of shear in Fig. 2 can be attributed to oscillations.

The existence of an anomalous loss mechanism independent of oscillations is best illustrated by Fig. 3. Here, we show oscillations of plasma density (actually, probe current) vs radius. The width of the trace is an indication of oscillation amplitude. The oscilloscope responds to all frequencies from dc to 1 MHz. As the shear is increased by varying the current I_s, the oscillation amplitude decreases, and the average density rises. At the low magnetic field of 2 kG, the oscillations are completely suppressed for all $I_s > 200$ A; yet the density continues to increase with I_s. This indicates that at low shear there is a loss mechanism which is either strictly dc or connected with very high frequencies. It is difficult to see how ions can be moved rapidly across the magnetic field by high frequencies,[24] and so we are led to the concept of plasma convection.

That large dc drifts should occur in the plasma if the temperature of the end plates is slightly nonuniform was actually predicted several years ago.[25] Asymmetric potentials connected with temperature gradients were first observed by Hartman and Munger.[26] The basic reason is that the plasma potential on each line of force is determined by the balance between flux of electrons emitted by the end plate and that of electrons drifting back into it; the sheath drop is an adjustable Coulomb barrier which insures this balance. Since thermionic emission is a steep function of temperature, a small temperature gradient in the end plate will cause a relatively large gradient in the sheath drop, and hence a potential gradient in the plasma. The resulting $\mathbf{E} \times \mathbf{B}$ drift will carry particles radially if T_e is azimuthally nonuniform. A variation of less than 1% in T_e is

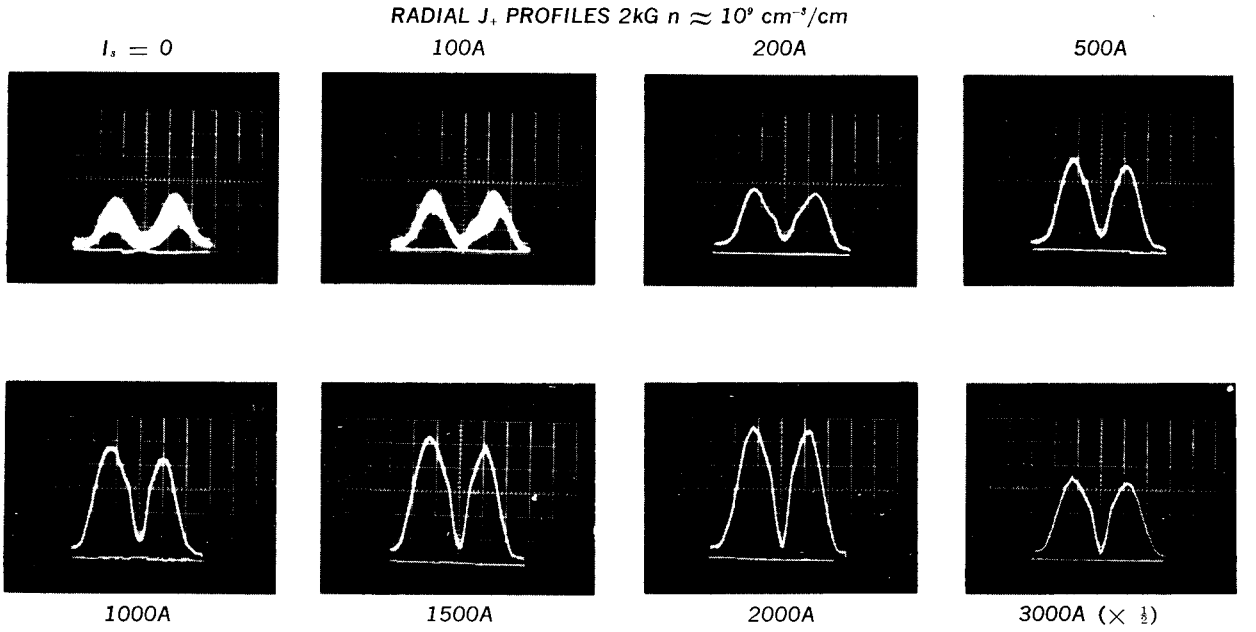

FIG. 3. Time-resolved density profiles at 2 kG as a function of shear. I_s is the current in the hard core. The density depression at the center is due to the presence of the hard core; the probe just grazes it. The probe current is dc coupled, and the baseline is shown.

sufficient to give a drift velocity comparable to the velocity of Bohm diffusion.[25]

Transport of plasma by steady $\mathbf{E} \times \mathbf{B}$ drifts was first observed by Bohm *et al.*[27] in an electric arc. In alkali plasmas, Decker *et al.*[18] were the first to point out that the observed loss rate was consistent with the drift mechanism described above; however, no detailed study of the electric field distribution was reported. By using shear, in the present work we are able to show that the conclusion drawn by Decker *et al.*[18] is basically correct. In low-β toroidal thermonuclear fusion devices, there are no end plates to cause dc electric fields, but these can arise from other causes. For instance, the method of plasma injection or heating has been shown to give rise to convective patterns in a toroidal octopole[28] and in a linear quadrupole.[29] The relevance of our experiment to fusion research lies in the prediction of the rate at which shear can be expected to reduce convective losses, whatever their cause.

In the present paper we establish the existence of convective patterns by measuring the plasma potential distribution and showing that it changes with shear in the expected manner. Furthermore, we present a theory of convection in sheared fields which correctly predicts the observed increase in confinement with shear. In this work we are concerned primarily with quiescent plasmas with finite shear; discussion of oscillation-induced losses is deferred to another paper.

II. APPARATUS

A. Magnetic Field

A diagram showing the vacuum and magnetic field features of the machine is shown in Fig. 4. The 0–4 kG B_z field is uniform to $\pm 1\%$ over the 6.6 liter plasma volume and is kept constant to $< 0.1\%$ by a transistor regulator. The hard core is a 1 cm diam water-cooled alumimun tube capable of carrying up to 5 kA dc; however, I_s is limited to about 4 kA by evaporation of condensed neutral potassium from the warm end of the tube, an effect which changes the magnitude and symmetry of the input ion flux. To counteract thermal expansion, the hard core is kept under 400 kg of tension by the lever and counterweight arrangement shown. Aluminum was chosen because its combination of weight, tensile strength, and conductivity was optimal; furthermore, its surface could be anodized to form an insulating layer, which prevents the dc potential drop along the tube from contacting the plasma. The sag of the hard core under gravity was negligible, but the force from the return leads limited the straightness of the tube to ± 0.2 mm. The hard core is threaded through 1.27-cm-diam holes in the hot plates and is kept centered in the holes by the supports shown.

B. Vacuum

The copper vacuum chamber is water cooled to keep the pressure of neutral K to $\leq 10^{-8}$ Torr.

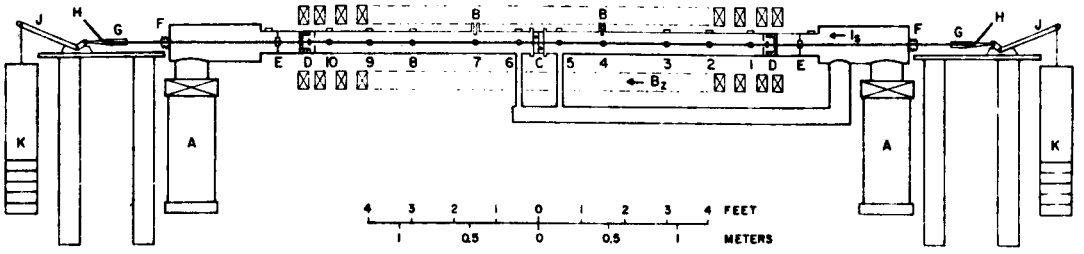

FIG. 4. Scale drawing of experimental layout: (A) diffusion pumps with freon baffles and pneumatic valves; (B) liquid N_2 traps; (C) center section with rotating probe mounts, replaceable with standard port cross; (D) hot plate assembly and aperture limiter; (E) hard-core support; (F) bellows and Viton O-ring seal for hard core; (G) clamp and electrical connection to hard core; (H) water inlet and outlet; (J) lever with 10-to-1 ratio; (K) lead weights. The port locations are numbered.

Viton O-rings are used throughout. Base pressure averages 2×10^{-6} Torr.

C. Hot-Plate Assembly

The ionizer plates are 6.35-cm-diam tungsten disks 1.3 cm thick, with a central hole 1.27 cm in diameter. They are heated by electron bombardment. The operating temperature is typically 2500° K, sufficient to create an electron sheath for the densities $n < 2 \times 10^{11}$ cm^{-3} encountered in the experiment. An aperture limiter sets the plasma radius at 2.54 cm. Details of the coaxial hot-plate structure are presented elsewhere.[30] Although a temperature uniformity of ±5° K is possible with this design, no particular effort to achieve optimum uniformity was made in this experiment, and the temperature varied typically by ±15° K. The distance between hot plates was 326 cm.

D. Oven and Collimator

The flux of neutral K atoms impinging on the hot plates is controlled by varying the temperature of the ovens in which vacuum-distilled metallic potassium is evaporated. Heated pipes carry the K vapor into the stainless steel collimator manifold.

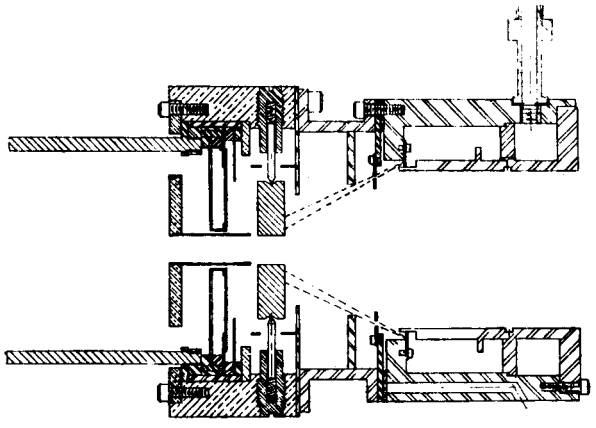

FIG. 5. Drawing of Type I beam collimator and hot-plate assembly.

Two types of beam collimators were used. Early work was done with Type I, shown in Fig. 5. The incoming K vapor is distributed azimuthally in the high-pressure chamber at the right and is bled into the low-pressure chamber at the left via small holes. Collimation of an annular beam is done by means of two annular slits. In the low-pressure chamber, the mean free path is long compared with the chamber dimensions at all pressures used. This method assures azimuthal symmetry and constancy of beam profile at all neutral fluxes. However, the radial collimation was difficult to control. In most of this work, Type II collimators, shown in Fig. 6, were used. Here, the neutral beam is directed at the hot plate by 16 small molybdenum tubes equally spaced in azimuth and aimed at a circle about midway between the hard core and the radius of the aperture limiter. Measurements made with Type I collimators were similar to the Type II data but showed a large ion input flux near the hard core and, consequently, a predominance of inward radial losses.

The ion input fluxes from the two ends of the machine were balanced to 5% before each run in order to minimize unidirectional drifts along the axis.

E. Probes

Coaxially shielded Langmuir probes of two designs were used for all local measurements. Type I has a

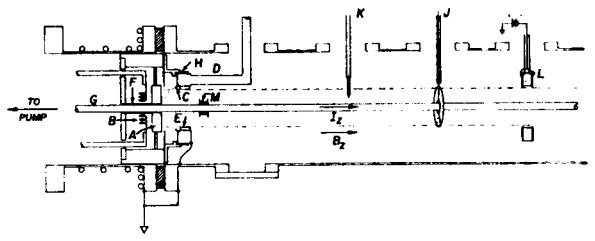

FIG. 6. Detailed drawing of ionizer and diagnostics: (A) hot plate; (B) filament; (C) atomic beam collimator; (D) heated pipe from oven; (E) aperture limiter; (F) grounded shield; (G) hard core; (H) collimator positioner; (J) flux collector; (K) probe; (L) radial flux detector; (M) inner aperture limiter and radial flux detector (not normally used).

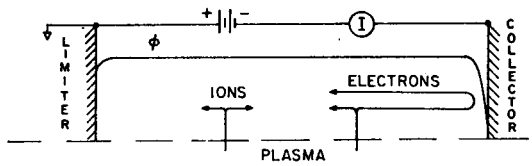

FIG. 7. Potential distribution and particle flow in the region outside the main plasma. Half of the machine is shown.

shield made of stainless steel hypodermic needle tubing and coated with epoxy to an over-all diameter of 0.38 mm. Type II has a shield consisting of a layer of silver paint between coaxial glass capillary tubes and has an over-all diameter of 0.25–0.30 mm. Type II is more fragile but can be positioned more accurately near the hard core; Type I suffers from the residual magnetism of the shield. Both types have cylindrical tungsten tips 0.05 mm in diameter and about 1 mm long; for fine structure measurements the tip is shortened to 0.1 mm. Details of probe construction are given elsewhere.[31,32]

The probes are moved radially by a variable-speed motor, and a radial scan can be plotted on an x-y recorder in about 30 sec. Scans of an entire plasma cross section are made by tilting the direction of travel about an axis 12.4 cm away from the axis of the machine. In normal operation the axis of probe motion is tilted slightly so that the probe just grazes the hard core. At the midplane (see Fig. 4) we sometimes used a probe mount on which two probes could be moved independently in the θ direction. This is done by manually rotating short sections of the vacuum chamber on sliding O-ring seals.

Since estimates of classical diffusion and recombination depend on the absolute value of plasma density, we calibrated the ion currents from such probes against densities measured by microwaves. This calibration is published elsewhere.[31]

The probe tips are normally covered with a layer of potassium. Slight changes in the work function of the surface can cause slow drifts in the apparent floating potential. In Sec. V we shall show how these drifts are subtracted out. As an additional check, we have used hot probes, consisting of a small loop of wire heated by dc, which are hot enough to keep off the layer of potassium but not hot enough to emit electrons. Use of these probes has verified the existence of asymmetric potential distributions.

F. Particle Collectors

The input ion flux Φ is measured by dropping the cold plates J (Fig. 6), which are split so that they can enclose the hard core. These plates are inserted at ports 2 and 9 (Fig. 4) and biased to -22 V to collect all ions emitted from the hot plates. Radial losses occurring between the hot plate and port 2, say, are eliminated by increasing I_s until the collected ion current saturates. With the cold plates in place, the distribution of input ion flux is measured by probes in ports 1 and 10. Because of radiation from the hot plates, these probes had to have alumina insulators, without shield.

The outward radial flux Φ_R is measured with the collector L shown in Fig. 6. It is placed near the midplane of the machine and has an inside diameter about an ion Larmor radius larger than the aperture limiter. It is biased negatively to collect ions and is split into four semicircular sections so that the symmetry of the radial losses can be checked. The theory of operation of this "plasma eater" is illustrated in Fig. 7. The plasma in the exterior region must be positive relative to the limiter and collector because of the large mobility of electrons along $\mathbf{B}$. In the absence of resistivity, the potential drops occur only in the sheaths. Ions entering the exterior region, therefore, see no longitudinal electric field; half of them recombine at the limiter and half at the collector. At saturation, the sheath on the collector is sufficient to repel all electrons; these flow only to the limiter. What flows through the ammeter are only those electrons needed to neutralize the ions flowing to the collector. Thus, the total radial ion flux is equal to *twice* the current flowing to all sections of the collector. The effect of the collector voltage on the plasma is removed by extrapolating the current to zero voltage. Note that this is an integrated measurement of all radial ion losses, as contrasted with the method of Buchel'nikova,[16] which samples only a small fraction of the plasma surface. The inner plasma eater M (Fig. 6) was used only for the measurement of Sec. VI D.

G. Alignment

The collimator positioner H (Fig. 6) and the smallness of the hole in the hot plate assure that the hard core is centered relative to the aperture limiters to within 0.5 mm. To align the hard core with the magnetic field, it is only necessary to align the aperture limiters with $\mathbf{B}$. At the radius of the limiter, there is a sharp rise in plasma potential due to the discontinuity in sheath drop and in work function at the ends of the machine. The location of this discontinuity is noted with two floating probes 90° apart near the midplane, first with one cold plate J (Fig. 6) inserted and then with the other. The entire vacuum chamber is moved until the

discontinuities from the two ends of the machine coincide within 0.5 mm.

III. THE PHYSICAL MODEL

The existence of an oscillation-independent loss mechanism is shown quantitatively in Fig. 8. The experimental points are the measured values of peak plasma density n_p for various values of I_s at constant B_z and ion input flux Φ. All the points lie well below n_{cl}, the density expected if only classical losses were present. The amplitude of low-frequency oscillations was measured at the same time. From this amplitude one can calculate[33] an upper limit to the radial transport due to the oscillations by assuming that the density perturbation n_1 and the drift velocity in the perturbed electric field E_1/B are exactly in phase. This gives a lower limit, n_{osc}, to the peak density one would expect if oscillations were the sole cause of the losses. Note that n_{osc} rises sharply up to $I_s \approx 200$ A, indicating stabilization of large oscillations. For $I_s \leq 200$ A, n_p is above or about equal to n_{osc}, indicating that oscillations could indeed be a primary loss mechanism. However, for $I_s > 200$ A, n_{osc} lies considerably higher than the experimental points, indicating that the oscillation amplitude is much too small to account for the losses. Moreover, whatever is limiting the density seems to be shear dependent. The theoretical curve on Fig. 8 shows the density expected from plasma convection, according to the theory to be presented in Sec. IV. Note that at zero shear the theoretical density is about twice the measured one, indicating that losses from convection and from oscillations are about equal in this case.

We, therefore, must find a loss mechanism which is sensitive to shear and exists in the absence of oscillations. One possibility is that end-plate recombination is anomalously large and is decreased by shear because the increase in the length of the lines of force increases the time of flight of ions to the end plates. This hypothesis fails on two counts. First, the magnitude of the effect is two orders of magnitude too small. At $r = 1.25$ cm, the radius of the density maximum, $rd\theta/dz$ for a line of force is 0.32 at $I_s = 4$ kA, $B_z = 2$ kG. Taking the Pythagorean sum $ds^2 = dz^2 + r^2\,d\theta^2$ brings the effect down to a 5% lengthening of the line of force, whereas a factor of 5 is needed to explain the shear dependence. Second, a recent direct measurement[34] of the end-plate recombination rate in a Q machine showed that it was within a factor of 2 of the expected value at $n = 10^{10}$ cm^{-3}; this is insufficient to explain the departure of n_p from n_{cl} in Fig. 8.

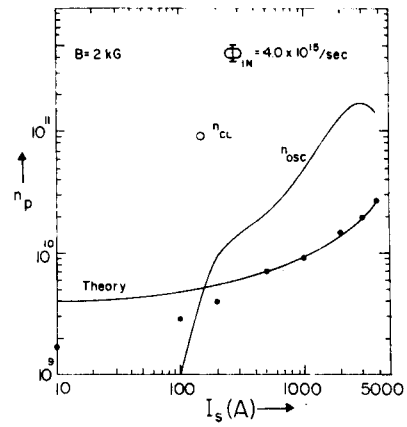

FIG. 8. Peak plasma density n_p vs hard-core current I_s at $B_z = 2$ kG. The curve n_{osc} is a lower limit to the peak density expected if oscillations were the cause of plasma losses. The point n_{cl} is the density expected from classical diffusion and end-plate recombination. The theoretical curve shows shear dependence of n_p calculated from the theory of convection given in this paper.

A suggestion[35] that charge exchange can cause anomalous losses also fails on two scores. First, we used potassium rather than cesium, and the partial pressure of neutral K is too small for this to be an important effect. Second, charge exchange would not be shear dependent.

However, consider the following hypothesis.[36] Suppose one of the end plates has an $m = 1$ azimuthal asymmetry in its temperature distribution. According to the well-known sheath conditions for a thermionic plasma,[25] there will then be an $m = 1$ asymmetry in the plasma potential ϕ at the sheath edge. Because of the good electrical conductivity, we may assume that ϕ is constant along each line of force. In the absence of shear, a typical equipotential will look like the off-center circle in Fig. 9 at any cross section in the plasma. With finite shear, the

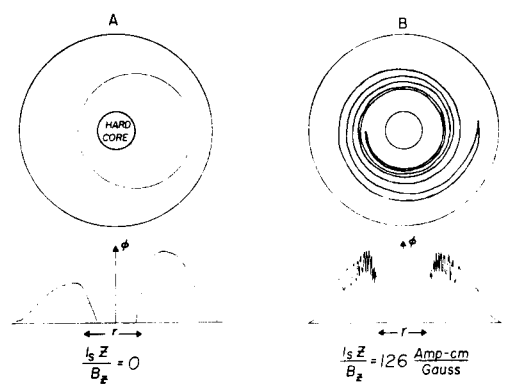

FIG. 9. Schematic of how an off-center equipotential at zero shear (A) is twisted into a long spiral at large shear (B). All other equipotentials are, of course, similarly twisted. The corresponding radial potential profiles are shown below.

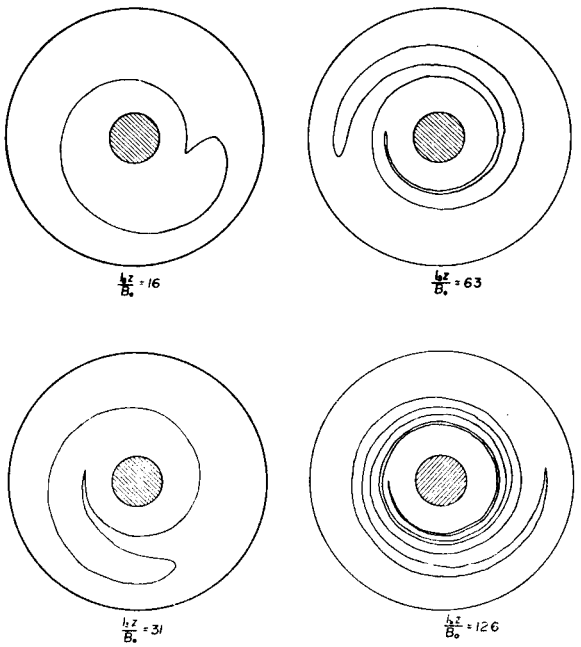

FIG. 10. Intermediate stages in the development of the spiral convective pattern of Fig. 9.

given equipotential will still have the same shape at the sheath edge but will be progressively distorted, as shown in Fig. 10, at cross sections farther and farther away from the nonuniform end plate. This is due to the differential rotation of the lines of force at different radii.

Particles $\mathbf{E}\times\mathbf{B}$ drifting along the asymmetric equipotentials will be able to change their radial positions without crossing the lines of force and thus appear to suffer from enhanced radial transport. With large shear, the particles will spend part of the time in cross sections where the length of the drift path is greatly increased, and their radial transport will appear to be decreased. Actually, in the spiral patterns, the increase in $\mathbf{E}$ exactly cancels the effect of the increase in drift path in the $r_L = 0$ limit. It is only finite Larmor radius effects that give the improvement in confinement. The theory for this will be presented in the next section. Experimental verification of the model and further refinements in the model will be presented in Secs. V and VI.

IV. THEORY

A. Fluid Approximation

We consider a semi-infinite cylindrical plasma with a given potential distribution at $z = 0$ and wish to compute the potential distributions at various cross sections $z \neq 0$ when a shear field B_θ is applied to the uniform field B_z. To do this, it is sufficient to use the fluid equations without resistivity, viscosity, $\mathbf{v}\cdot\nabla\mathbf{v}$, or finite Larmor radius. Modifications due to these effects will be considered later. The presence of a second end plate at which a different potential distribution is produced by thermal gradients will also be taken into consideration later. The steady-state equation of motion for ions and electrons is then

$$q_i n(\mathbf{v}_i\times\mathbf{B} - \nabla\phi) - KT\nabla n = 0, \quad j = i, e. \tag{1}$$

Here, we have assumed that the plasma is isothermal and quasineutral. Taking the scalar product of Eqs. (1) with $\mathbf{B}$, we see immediately that ϕ and n are constant along a line of force in this approximation. Defining

$$v_s = \left(\frac{KT}{M_i}\right)^{1/2}, \qquad \omega_c = \frac{eB_z}{M_i}, \qquad a_i = \frac{v_s}{\omega_c},$$

$$\eta = \frac{e\phi}{KT}, \qquad \psi_{i,e} = \eta \pm \ln n,$$

we rewrite Eq. (1) as

$$\frac{\mathbf{v}_j\times\mathbf{B}}{B_z} = a_i v_s \nabla\psi_j. \tag{1'}$$

When B_θ is produced by a hard core, and $(\hat{e}_r, \hat{e}_\theta, \hat{e}_z)$ defines the cylindrical coordinate system, $\mathbf{B}$ is given by

$$\frac{\mathbf{B}}{B_z} = \hat{e}_z + \left(\frac{2I_s}{rB_z}\right)\hat{e}_\theta = \hat{e}_z + \left(\frac{\alpha}{r}\right)\hat{e}_\theta, \tag{2}$$

where

$$\alpha \equiv \frac{2I_s}{B_z}\ (\text{abA/G}).$$

The r, θ, and z components of Eq. (1′) then become, respectively,

$$v_{i\theta} - \left(\frac{\alpha}{r}\right)v_{iz} = a_i v_s\left(\frac{\partial\psi_i}{\partial r}\right), \tag{3}$$

$$v_{ir} = -\left(\frac{a_i v_s}{r}\right)\left(\frac{\partial\psi_i}{\partial\theta}\right), \tag{4}$$

$$\left(\frac{\alpha}{r}\right)v_{ir} = a_i v_s\left(\frac{\partial\psi_i}{\partial z}\right). \tag{5}$$

The last two equations yield

$$\psi_i = \psi_i(r, \theta - \alpha z r^{-2}), \tag{6}$$

so that ψ_i is constant along a line of force.

It will be apparent that the experimentally observed potential distributions can be approximated by

$$\eta(z = 0) = f(r) + g(r)\sin m\theta, \tag{7}$$

where $f(r)$ is the normal, symmetric potential profile and $g(r)$ is the small asymmetric part caused by end-plate temperature inhomogeneities. Both f and g vary on the scale of the plasma radius. From Eqs. (6) and (7), we have

$$\eta(r, \theta, z) = f(r) + g(r) \sin m(\theta - \alpha z r^{-2}), \quad (8)$$

so that

$$\eta(r + \Delta r, \theta, z)$$

$$= f(r + \Delta r) + g(r + \Delta r) \sin m\left(\theta - \frac{\alpha z}{(r + \Delta r)^2}\right)$$

$$\approx f(r) + g(r) \sin m\left(\theta - \frac{\alpha z}{r^2} + \frac{2\alpha z}{r^3}\Delta r\right). \quad (9)$$

Thus, when αz is large, a small change in r can cause a change of 2π in the argument of the sine, giving rise to spatial oscillations in η. Equations (8) and (9) describe the spiral pattern and radial potential profile shown schematically in Fig. 9B. Equation (9) predicts that the amplitude of the spatial potential oscillations, which we shall henceforth call "ripples," is given by $g(r)$, and that the spacing between ripples is

$$\Delta r = \frac{\pi r^3}{m\alpha z}. \quad (10)$$

We next wish to compute the increase in confinement time associated with the twisting of the drift surfaces. We assume $\psi_i(z = 0)$ to have the form of Eq. (7). For clarity we shall consider the case $m = 1$; a similar argument will hold for arbitrary distributions $\eta(z = 0)$. In the absence of shear, an ion-fluid element can make an excursion in radius by drifting along an off-center equipotential (see Fig. 9A). From Eq. (4), the time required to drift from, say, the minimum to the maximum radius covered by a given equipotential is

$$\Delta t = \int_{r_{min}}^{r_{max}} \frac{dr}{v_r} = \frac{1}{a_i v_s} \int_{r_{min}}^{r_{max}} \frac{r\, dr}{[\partial\psi_i/\partial\theta]_{\theta = F}} \quad (11)$$

where the integrand is to be evaluated following the fluid element; that is, at

$$\theta = F(\psi_i, r), \quad (12)$$

a relation found by inverting $\psi_i(z = 0) = f(r) + g(r) \sin \theta$. Clearly, θ is double valued, and we must choose the branch corresponding to $v_r > 0$. When $I_s = 0$ Eq. (11) is independent of z. However, with finite I_s, we must take Eq. (8) for the form of ψ_i and invert it to give

$$\theta = G(\psi_i, r, z) \quad (13)$$

which is to be used in Eq. (11) in place of Eq. (12). It is convenient to transform to the helical coordinate system suggested by Eq. (6):

$$r' = r, \qquad u = \theta - \alpha z r^{-2}, \qquad z' = z. \quad (14)$$

Equations (5), (4), and (3) become, respectively,

$$\frac{\partial\psi_i}{\partial z'} = 0, \quad (15)$$

$$\frac{dr'}{dt} = -\left(\frac{a_i v_s}{r'}\right)\left(\frac{\partial\psi_i}{\partial u}\right), \quad (16)$$

$$r'\left(\frac{du}{dt}\right) = a_i v_s \left(\frac{\partial\psi_i}{\partial r'}\right). \quad (17)$$

Now we have $\psi_i = f(r') + g(r') \sin u$, which can be inverted to give $u = F'(\psi_i, r')$. With the use of Eq. (16), the time Δt for finite I_s and z is given by

$$\Delta t = -\frac{1}{a_i v_s} \int_{r'_{min}}^{r'_{max}} \frac{r'\, dr'}{[\partial\psi_i/\partial u]_{u = F'}}. \quad (18)$$

Comparing this with Eq. (11), we see that the two equations are the same, for (a) the limits of integration are the same, since the transformation is radius preserving, (b) ψ_i is the same function of u in Eq. (18) as ψ_i is of θ in Eq. (11), and (c) F' is the same function of r' as F is of r. Thus, the transport rate is unchanged by shear.

This confirms our previous intuitive statement that the effect of the increase in drift-path length is nullified by an increase in drift velocity. However, it is well known that ions drifting in a nonuniform electric field have a smaller velocity than E/B. This finite-Larmor-radius effect will become important when the shear twists the equipotentials into spirals with a ripple spacing comparable to a_i.

B. Finite-Larmor-Radius Effects

We shall give a rough estimate of the finite-Larmor-radius effect, followed by a sketch of the detailed calculation, which will be given in the Appendix. Consider a single ion drifting in a potential distribution of the form of Eq. (8). In the absence of shear ($\alpha z = 0$), we have $\eta = f(r) + g(r) \sin \theta$ for $m = 1$. The velocity with which the guiding center of the ion makes an excursion δr from r_{min} to r_{max} is given by

$$v_r = \frac{E_\theta|_{av}}{B} = \frac{1}{r}\frac{KT}{eB}\left[\frac{\partial\eta}{\partial\theta}\right]_{av}$$

$$= \frac{1}{r}\frac{KT}{eB} g'(r) [\cos\theta]_{av}$$

where $[\cos\theta]_{av}$ is the average over the drift path

Dropping this factor to get an order of magnitude estimate, we have

$$|v_r| \approx \frac{1}{r}\frac{KT}{eB}\, g(r). \tag{19}$$

When αz is large, the drift path will be twisted into a long spiral (Fig. 9B), and the guiding center will make the excursion δr by drifting along the spiral with a velocity v_θ. From Eq. (8), we have

$$v_\theta = -\frac{[E_r]_{av}}{B} = \frac{KT}{eB}\left[\frac{\partial \eta}{\partial r}\right]_{av}$$
$$= \frac{KT}{eB}\frac{2\alpha z}{r^3}\, g(r)\left[\cos\left(\theta - \frac{\alpha z}{r^2}\right)\right]_{av}.$$

However, when the ripple spacing is not large compared to the Larmor radius, this drift velocity is decreased by the well-known[37] factor $(1 - \frac{1}{2}k_r^2 a_i^2)$. This finite-Larmor-radius correction factor is applicable for $E_r \sim \sin k_r r$ and $\eta \ll 1$. Again dropping the cosine factor, we have

$$v_\theta \approx \frac{KT}{eB}\frac{2\alpha z}{r^3}\, g(r)(1 - \tfrac{1}{2}k_r^2 a_i^2). \tag{20}$$

The wavelength k_r is given locally by Eq. (10),

$$k_r \approx \frac{2\pi}{\Delta r} = \frac{2\alpha z}{r^3}. \tag{21}$$

The number of turns N in the spiral is, from Eq. (8), $N = \alpha z/2\pi r^2$. The length of the drift path is then, approximately, $\delta l \approx 2\pi r N = \alpha z/r$. The time required to go from r_{min} to r_{max} is $\delta t = \delta l/v_\theta$, and the radial drift velocity is, approximately, $v_r \approx \delta r/\delta t$. If $\delta r \approx r$, we have, roughly,

$$|v_r| \approx \frac{r}{\delta t} \approx \frac{r v_\theta}{\delta l} \approx \frac{r^2}{\alpha z}\frac{KT}{eB}\frac{2\alpha z}{r^3}\, g(r)(1 - \tfrac{1}{2}k_r^2 a_i^2)$$
$$\approx \frac{2}{r}\frac{KT}{eB}\, g(r)\left[1 - 2\left(\frac{\alpha z a_i}{r^3}\right)^2\right]. \tag{22}$$

Comparing this with Eq. (19), we see that the effect of shear has canceled out, as expected, except in the factor in brackets arising from the finite-Larmor-radius effect.

To calculate v_r rigorously from kinetic theory, we consider the motion of a fluid of guiding centers. This is appropriate for our purposes because the diamagnetic drifts which occur in a real fluid, being perpendicular to the density gradients, cannot contribute to losses. For simplicity, we employ a slab model, with

$$\mathbf{B} = B_z[\hat{e}_z + \gamma(x)\hat{e}_y]. \tag{23}$$

The equations of motion for a single ion are then

$$\frac{d(\mathbf{v}/v_s)}{d(\omega_c t)} = -a_i\nabla\eta + \frac{\mathbf{v}}{v_s}\times(\hat{e}_z + \gamma\hat{e}_y), \tag{24}$$

$$\mathbf{v} = \frac{d\mathbf{x}}{dt}. \tag{25}$$

To solve Eq. (24) by expansion, we require $|a_i\nabla\eta| \ll 1$, which is not generally true, since $\eta \gtrsim 1$ in the plasma, and $k_r a_i \gtrsim 1$ in the twisted spirals. Fortunately, we can break η into two parts:

$$\eta(\mathbf{x}) = \eta_0(x) + \eta^{(1)}(x, y, z), \tag{26}$$

where η_0 represents the symmetric distribution in the cylindrical case, and $\eta^{(1)}$ is the asymmetric part. Now, η_0 can be $\gtrsim 1$, but it varies on the scale of $R \gg a_i$; $\eta^{(1)}$ can vary on the scale of a_i in the ripples, but it is found experimentally that $|\eta^{(1)}| \ll 1$.

Thus, we devise the following ordering scheme. Let $\epsilon = a_i/R$, where R is the scale on which η_0 varies. We assume

$$\frac{a_i\,\partial\eta_0}{\partial x} = O(\epsilon), \quad \frac{a_i\,\partial\eta^{(1)}}{\partial x} = O(\epsilon), \quad \frac{a_i\,\partial\eta^{(1)}}{\partial y} = O(\epsilon^2). \tag{27}$$

We also make the reasonable assumption that $\gamma(x)$ is small but the scale length in z is large, so that γz can be large and the spiral patterns well developed. Thus, we take

$$\gamma(x) = O(\epsilon), \quad \frac{a_i\,\partial\eta^{(1)}}{\partial z} = O(\epsilon^3). \tag{28}$$

Finally, we make a multiple time-scale expansion

$$\frac{d}{dt} = \omega_c\frac{d}{d\tau} + \epsilon\omega_c\frac{d}{d\tau_1} + \epsilon^2\omega_c\frac{d}{d\tau_2} + \cdots, \tag{29}$$

where $\tau = \omega_c t$, τ_1 varies on the scale of $(\epsilon\omega_c)^{-1}$, etc. The τ scale is that of cyclotron gyration, and the other terms describe the drift of the guiding center.

With this ordering scheme, Eqs. (24) and (25) are solved order by order in ϵ. In lowest order, only the cyclotron motion appears; this is removed by averaging over a gyration period. The harmless drift in the y (or θ) direction appears in first order. The radial drift first appears in second order. The effects of shear on v_z arise only in third order. Finally, an average must be taken over a Maxwellian velocity distribution. The details of this tedious calculation are given in the Appendix. For η of the form $\eta(\mathbf{x}) = \eta_0 + \eta_1(x)\sin k[y - \gamma(x)z]$, the result is

$$\bar{v}_x = -k\frac{KT}{eB}\eta_1(x)\cos k(y - \gamma z)$$
$$\cdot\exp\{-\tfrac{1}{2}[ka_i z\gamma'(x)]^2\}, \tag{30}$$

$$= B^{-1}E_y(x_0, y_0, z = 0)$$
$$\cdot \exp\{-\tfrac{1}{2}[ka_i z\gamma'(x_0)]^2\}, \qquad (31)$$

where $\bar{v}_x$ is the x component of the guiding center drift velocity, averaged over a Maxwellian distribution, for ions whose guiding centers lie on a line of force which goes through the point (x_0, y_0) at $z = 0$. Thus, the effect of shear, given by $\gamma'(x) \equiv \partial\gamma/\partial x$, is to decrease the "radial" drift velocity exponentially as z increases.

To compare with our previous result, we may put Eq. (30) into cylindrical coordinates with the substitutions $k \to m/r$, $x \to r$, $y \to r\theta$, $\gamma \to \alpha/r$, $\eta_1(x) \to g(r)$. Specializing to $m = 1$ and dropping the cosine factor, we obtain

$$|\bar{v}_r| = \frac{1}{r}\frac{KT}{eB}\, g(r) \exp\left[-\frac{1}{2}\left(\frac{\alpha z a_i}{r^3}\right)^2\right]. \qquad (32)$$

When the exponential is expanded, this has the same form as the rough estimate Eq. (22) and differs only by some numerical constants arising from the proper averaging over the drift path and over the distribution function.

C. Computation of the Loss Rate

To apply the above result to experiment, we must have a picture of how particles are lost from the plasma column, and we propose the following one. Electrons can be lost easily to the end plates, but the sheath drop there confines the ions, and they must be lost radially. Let $r = a$ be the radius of the hard core (more accurately, the radius of the holes in the end plates), and $r = b$ the radius of the aperture limiter. When an ion $\mathbf{E} \times \mathbf{B}$ drifts to $r < a$ or $r > b$, it has a finite probability of striking a cold surface and recombining before it can drift back into the column. This probability depends on the transit time along $\mathbf{B}$ to the ends of the machine. In fact, the guiding center needs to drift only to within a Larmor radius of a or b for the ion to be lost with a finite probability. Hence, the loss rate is proportional to the radial flux of ions at the loss radii $a_1 = a + r_L$ and $b_1 = b - r_L (r_L \equiv \sqrt{2}\, a_i)$.

In the absence of shear, ions drift along equipotentials with the velocity $\mathbf{E} \times \mathbf{B}$. If these equipotentials are not concentric with the hard core, some of them will cross the loss radii $r = a_1$ and $r = b_1$, and ions on these equipotentials will drift out of the column. According to Eq. (19), the radial component of the drift velocity depends only on the asymmetric part $g(r)$ of the potential distribution. However, not all equipotentials will cross $r = a_1, b_1$. Ions on the "confined" equipotentials cannot be lost by this convection process. The fraction of ions on "unconfined" equipotentials obviously depends on the radial excursion $\delta r = r_{\max} - r_{\min}$ made by a typical equipotential. By expanding Eq. (7), one can easily show that $\delta r \propto g/f'$. Thus, even if $g(r)$ is large, there is little convective loss if the equipotentials are made concentric by a large radial electric field.

It is a peculiarity of the present experiment that $f'(r)$ is not large, because of our efforts to achieve isothermal hot plates. Consequently, δr is not small relative to $b_1 - a_1$. Furthermore, the ion Larmor radius is such that it is easy for an ion on a confined equipotential to jump to an unconfined equipotential by making one or two collisions in a time short compared with the confinement time. Therefore we make the basic assumption, valid in our case but not in general, that *all the ions are on unconfined equipotentials*. When shear is applied, the equipotentials are twisted into spirals approximately concentric with the hard core. In the limit of large shear, an ion samples the potential asymmetry many times in a gyration and ends up with a nearly azimuthal drift. Ions farthest from the end plate will have the most symmetric drifts and will be confined the longest.

To compute the loss rate, we assume that the region $x \leq X$ is a sink for ions. The flux crossing the plane $x = X$ from above is then

$$\frac{dN}{dt} = \int_0^L dz \int_{v_x<0} [n(\mathbf{x})\bar{v}_x]_{x=X}\, dy, \qquad (33)$$

where dN/dt is the total number of ions entering the loss region per second from a plasma of length L. Here, $n(\mathbf{x})$ is properly the density of guiding centers but can be approximated by the measured ion density at the boundary. Substituting Eq. (30) for $\bar{v}_x$ and carrying out the integrations, we obtain

$$\frac{dN}{dt} = -\frac{kYL}{\pi}\frac{KT}{eB}\, n(X)\eta_1(X)\Gamma(X), \qquad (34)$$

where Y is the width of the plasma in the y direction, and

$$\Gamma(X) \equiv \left(\frac{\pi}{2}\right)^{1/2}\frac{1}{k\beta_L}\operatorname{erf}\left(\frac{k\beta_L}{\sqrt{2}}\right), \qquad (35)$$

$$\beta_L \equiv a_i\gamma'(X)L. \qquad (36)$$

Equation (34) has the expected dependences on n, η_1, and KT/eB. When $\beta_L = 0$ (no shear), $\Gamma(X)$ is equal to 1, and dN/dt can be comparable to the rate of Bohm diffusion when η is only 0.1. (Of course, we must eventually reduce dN/dt by the probability P of recombination once an ion reaches the radial boundary.) When β_L is large, Eq. (35) shows that the loss rate is reduced by shear by a factor $\sim \beta_L^{-1}$.

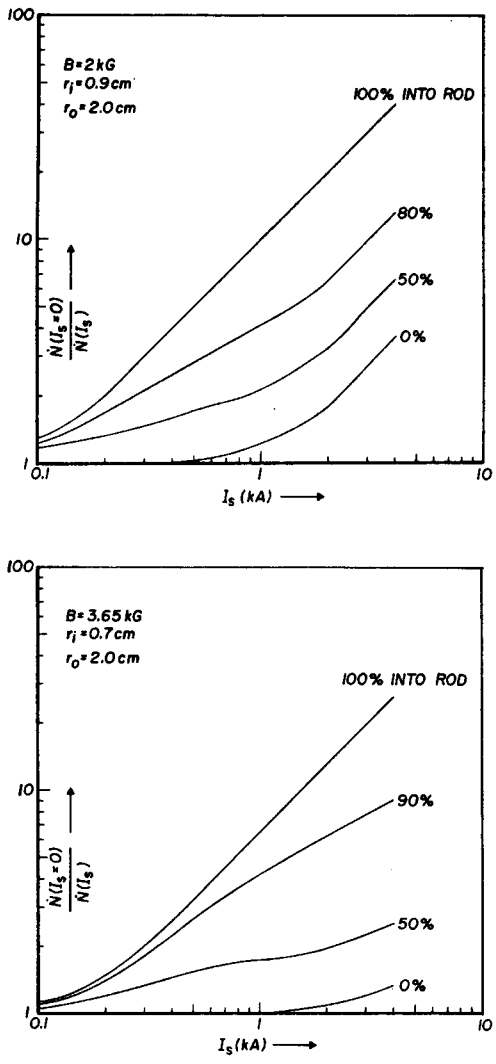

FIG. 11. Theoretical curves for the relative increase in confinement with shear for various ratios of losses to the inner ($r = r_i$) and outer ($r = r_o$) boundaries. I_s is the current in the hard core.

To apply the above result to experiment, we replace k with m/r, γ with α/r, Y with $2\pi r$, and X with a_1 or b_1. Since we have two radial boundaries, it is convenient to define $\dot{N}_a$ and $\dot{N}_b$ to be the loss rates to the hard core and to the aperture limiter, respectively. From Eq. (34) one then obtains the following useful formula:

$$\frac{\dot{N}(I_s)}{\dot{N}(0)} = \frac{\dot{N}_a(0)\Gamma(a) + \dot{N}_b(0)\Gamma(b)}{\dot{N}_a(0) + \dot{N}_b(0)}, \qquad (37)$$

where $\dot{N}(0)$ is the loss rate at zero hard-core current I_s. Theoretical curves for Eq. (37) are shown in Fig. 11 for various ratios $\dot{N}_a/\dot{N}_b$. This relative decrease of $\dot{N}$ with shear should not be sensitive to the probability P mentioned above.

V. EXPERIMENTAL TESTS OF THEORY

A. Single-Ended Operation

1. Convective Patterns

To test the predictions of the theory of Sec. IV, we first looked for the twisting of equipotential surfaces in single-ended operation, in which one of the cold plates was inserted to mask off one of the hot plates. The probe floating potential was then measured at various cross sections at different distances z from the hot plate. The entire cross section was probed by scanning along different chords as the direction of motion of the probe drive was progressively inclined. An entire scan took about 30 min, and although the power supplies were sufficiently well regulated to keep the plate temperature constant, the work function of the probe surface changed in this time. During a single "radial" trace, however, the work function did not drift appreciably. To normalize the various "radial" traces relative to one another, a calibration trace was taken in which the probe was swung quickly through the plasma in a direction perpendicular to the normal direction of motion. The various potential profiles were then cross plotted to give equipotential contours.

A typical result is shown in Fig. 12. In (A), three equipotential lines measured at Port 1 (Fig. 4)

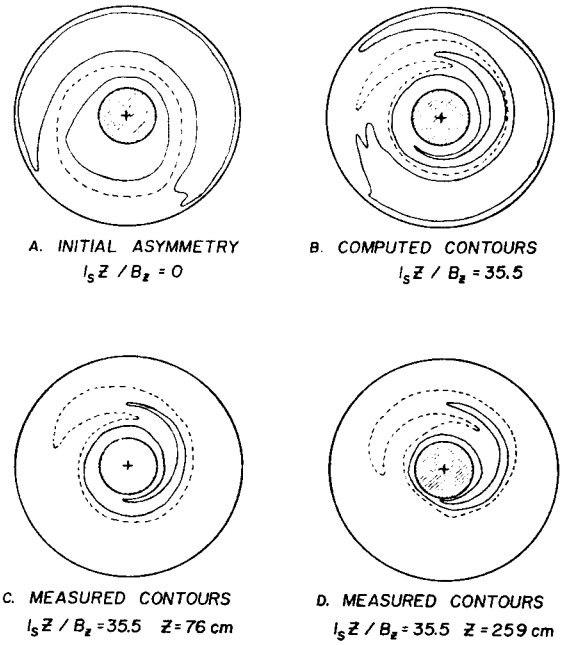

FIG. 12. Comparison between the computed and measured twisting of equipotential contours by shear. Data taken at low density and single ended. The dashed equipotential, for instance, represents the same absolute value of ϕ in each figure. Full explanation given in text.

with $I_s = 0$ are shown. This shows that the asymmetry is approximately an $m = 1$ distortion. According to Eq. (6), the equipotential contours should be constant for constant $\alpha z \propto I_s z/B_z$. In (B), the contours of (A) are shown as one would expect them to appear for $I_s z/B_z = 35.5$, according to Eq. (6). In (C) and (D) the contours actually measured for $I_s z/B_z = 35.5$ are shown for two cross sections at different distances from the hot plate. The measured contours have the same shape and orientation as that predicted by Eq. (6), indicating that the approximation that ϕ is constant along a line of force is a good one. The slight differences between (C) and (D) are probably caused by diffusion.

When the shear is large, complete plots of the equipotential contours become too difficult to construct. However, verification of the tight spiral pattern one expects from Fig. 9B and Eq. (6) can be made by taking the radial potential profiles at different values of shear. For this purpose, we used an especially short probe (0.1 mm length) and moved it along a true radius rather than along a chord grazing the hard core. Such a set of profiles is shown in Fig. 13 for a low value of B_z. One sees the development of the spiral pattern of Fig. 9B. At zero shear, one has mainly the azimuthally symmetric distribution $f(r)$, which varies slowly on the scale of $a_i = r_L/\sqrt{2}$ but has an amplitude greater than $KT = 0.22$ eV. The sharp rise in potential at the limiter is typical of Q machines and is due to the change in work function and sheath drop at the ends. At large shear, the asymmetric part of the potential varies sinusoidally with r, as predicted by Eq. (8). Note that the ripple spacing Δr increases with r because the shear decreases, and that the ripple amplitude is less than KT, as assumed in the theory. The potential can vary on a scale smaller than a_i because it is the electron Larmor radius which determines the lower limit to Δr. However, when $\Delta r < a_i$, the ripple amplitude is seen to decrease; this will be discussed later.

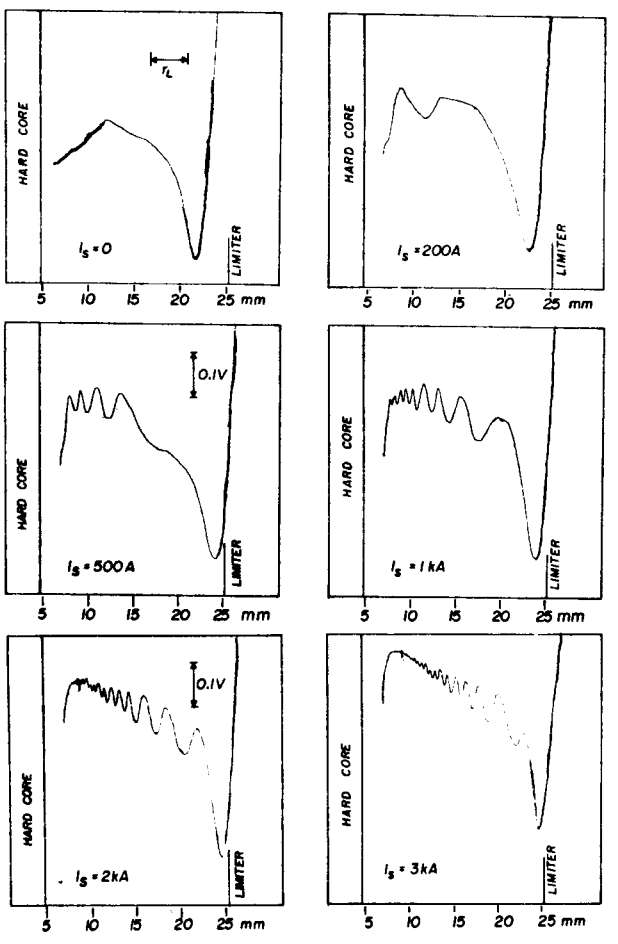

FIG. 13. X-y recorder traces of probe floating potential vs radius at the midplane as the current I_s in the hard core is increased. $B = 1$ kG, $n \approx 10^{10}$ cm^{-3}.

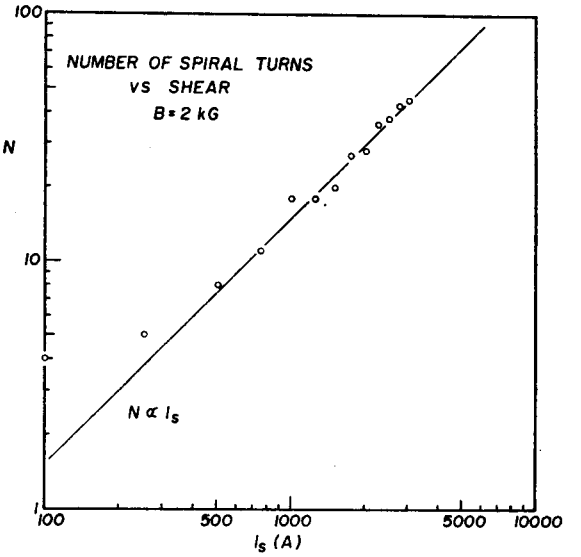

FIG. 14. Number of spiral turns, as indicated by the potential profiles, versus I_s.

From data such as these, one can check the predictions of Eq. (8). For instance, the total number of periods of the sine is clearly proportional to α and to I_s. This is demonstrated in Fig. 14. According to Eq. (10), the spacing Δr between ripples is proportional to r^3; this is shown in Fig. 15 for three values of B_z and two values of I_s. The lines are plots of Eq. (10) and have not been normalized to the experimental points. Similarly good agreement is found at other values of B_z and I_s. These data confirm the existence of the potential patterns postu-

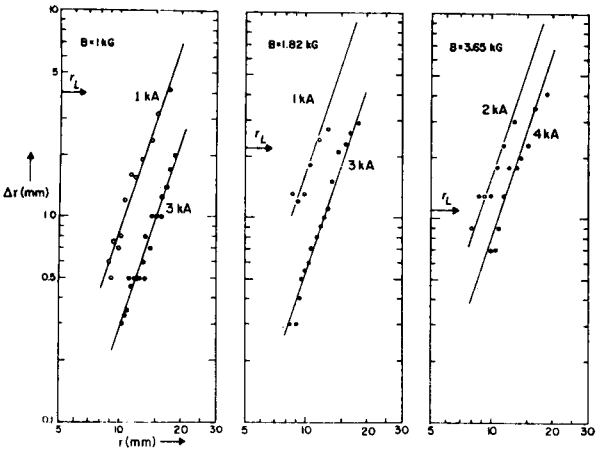

FIG. 15. The spacing Δr between spiral turns vs radius r. The points have not been normalized in any way.

lated in Sec. III to explain the dependence of the anomalous losses on shear.

2. *Plasma Confinement*

To test the predictions of the theory in regard to radial losses, we performed a single-ended experiment in which one hot plate was replaced by a segmented cold plate biased to collect ions. The innermost segment, surrounding the hard core, had a radius of 2.54 cm, the same as the aperture limiters. The middle segment, concentric with the first, had an outside radius of 5.08 cm and collected most of the ions that had drifted outside the main plasma column. The outermost segment was used to insure that ions did not drift so far as to be lost to the vacuum chamber walls; indeed, only 1% of the flux was collected on the outermost segment.

In this run, no inner plasma catcher was used, and the flux escaping inwards to the hard core was not measured directly. Instead, it was calculated by subtracting the flux to the segmented collector from the total input flux, as measured by the cold collector (Fig. 5J) inserted near the hot plate. Typical results are shown in Fig. 16. The theoretical curves are taken from the 0% and 100% curves of Fig. 11B, which predict separately the change in loss rate to the outside and to the rod, respectively. The absolute value has been adjusted to fit the experimental points, but it is clear that the variation with I_s is in reasonable agreement with experiment. This agreement supports our choice of the loss radii a_1 and b_1 in Sec. IVC. The small discrepancy between theory and experiment can be explained by the existence of higher m numbers than 1 in the potential asymmetry, and by stabilization of oscillations. The absolute value of radial losses can be estimated from

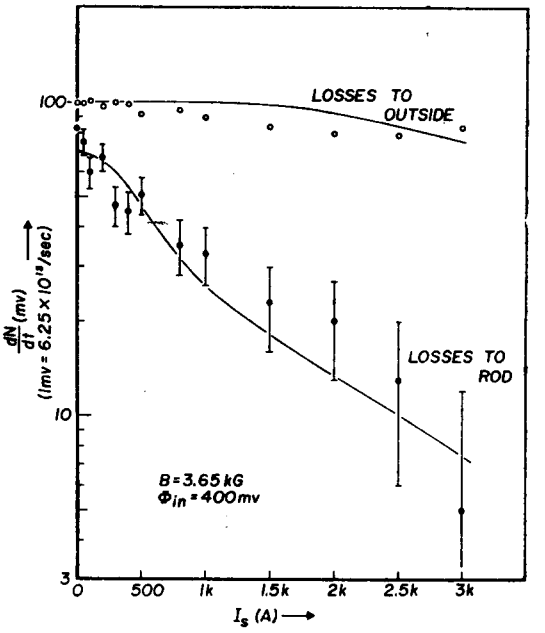

FIG. 16. Comparison of measured and calculated inward and outward radial losses as a function of shear in a single-ended experiment.

Eq. (34) by inserting reasonable values for the parameters. With $n = 10^{10}$ cm^{-3}, $\eta_1 = 0.2$, $k = m/r = 1/b_1$, $\Gamma = 1$, one obtains $\dot{N} \approx 6.5 \times 10^{15}$ sec^{-1} (100 mV), which is in agreement with the observed loss to the outside at $I_s = 0$. Note that the asymmetry was large enough in this case that 42% of the input flux was lost radially by convection by the time the ions reached the other end of the machine.

B. Double-Ended Operation

1. *Convective Patterns*

When both hot plates are used and they have different asymmetries in temperature, what will be the potential distribution in the plasma? If the resistivity is zero, a thermoelectric current will flow along each line of force which connects points of different temperature on the hot plates. If the resistivity is finite, the potentials at the sheath edges at the two ends of the line of force will be different, and this difference will drive a smaller thermoelectric current through the resistive plasma. When the resistivity is large, the potentials at each sheath edge will be as if the other end plate were at the same temperature, and the actual difference in sheath edge potentials will be uniformly distributed along the line of force. Thus, the potential distribution at any cross section should be an average of the distributions near each plate, weighted by the fractional distance of the cross section from that plate.

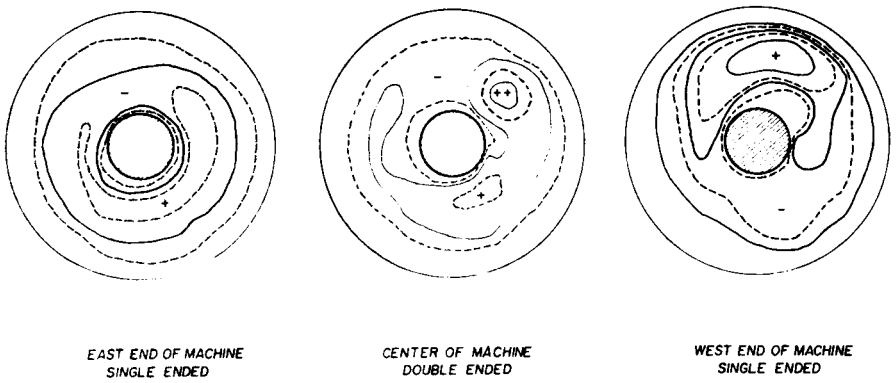

FIG. 17. Potential contours in double-ended operation, illustrating that the potential distribution is an average of those imposed by each plate. Note that although the asymmetries shown here are large because the radial and azimuthal gradients are of the same order of magnitude, the absolute value of the end-plate temperature gradient $\nabla T/T$ is only about 0.3%/cm.

Figure 17 represents an attempt to check this picture of double-ended operation in the case of zero shear. The potential distribution was measured at the midplane with first one and then the other plate heated alone. The distributions were indicative of the temperature asymmetries on each plate. When both plates were heated, the contours resembled neither single-ended distribution but were consistent with an average of the two distributions. For instance, the large positive island occurs where the potential maxima from the two ends overlap. A detailed analysis is not possible because large drift-type oscillations arise upon changing from single-ended to double-ended operation.

When shear is applied, the lines of force will connect points of different temperature on the end plates at different I_s. The resultant potential distribution at the midplane should still be an average of the twisted patterns established by each plate in the absence of the other. Figure 18 shows a radial potential profile in double-ended operation at high shear. It has the same feature as the single-ended profiles of Fig. 13, but the ripple pattern is more complex. Plots of Δr vs r for such double ended profiles are similar to Fig. 15 showing that the $\Delta r \propto r^3$ scaling and the absolute value of Δr are still in agreement with Eq. (10). These observations indicate that the picture of twisting of equipotentials under shear is still valid in double-ended operation.

2. *Plasma Confinement*

The relevance of this work to thermonuclear fusion becomes apparent in this section, in which we show the effect of shear on plasma convection when it is the primary cause of anomalous loss. In double-ended operation, ions are confined electrostatically by the electron sheaths on the end plates, so that axial loss is negligible for a machine the length of ours. The ions are then lost almost entirely radially, the way they are lost from a torus. We are then able to test the effect of shear on this loss without the confusing effect of toroidal curvature.

To compute the loss rate in double-ended operation, one should take $\eta(\mathbf{x})$ to be of the form $\eta(\mathbf{x}) = \eta_0(x) + \eta_1(x) \sin k[y - \gamma(x)z][(L - z)/L] + \eta_2(x) \sin k[y - \gamma(x)(z - L) + \Theta](z/L)$, in which we have weighted the asymmetries originating at $z = 0$ and $z = L$ in the manner indicated in the previous subsection. However, when this form is used, the expression for dN/dt, Eq. (34), cannot be expressed in closed form. Fortunately, a rather good approximation is suggested by the physical picture. Because

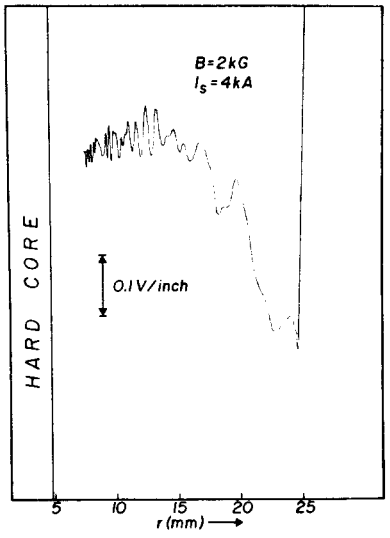

FIG. 18. X-y recorder trace of potential profile in double-ended operation.

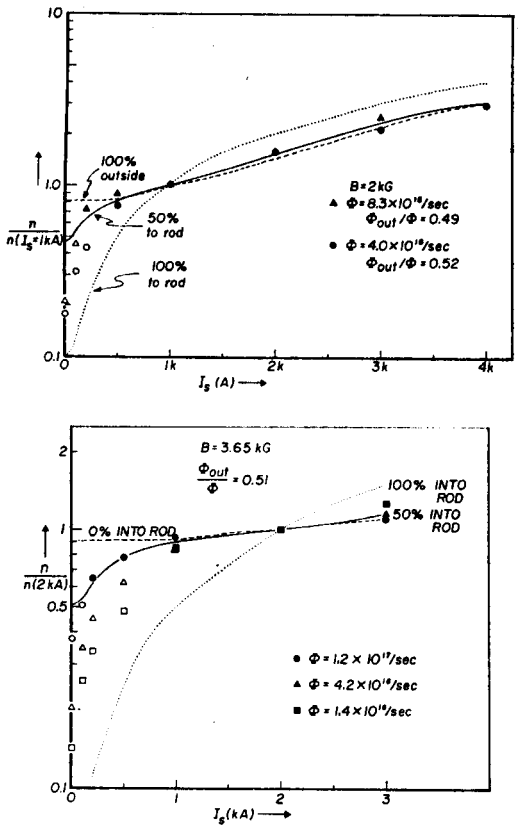

FIG. 19. The increase of peak density with shear for B_z = 2.0 and 3.65 kG. The points and curves have been normalized at I_s = 1 and 2 kA, respectively. The curves are the theoretical predictions for various ratios of inward to outward losses at I_s = 0; the measured ratios are indicated. The solid points indicate that the plasma is quiescent; the open points indicate that the confinement could be affected by oscillations.

the loss rate decreases with z as $1/z$ at large β_L [Eq. (35)], most of the losses at high shear occur near each end plate. At the midplane, the spiral patterns from both end plates are so well developed that little radial loss occurs. Thus, we may integrate the losses in z from each end plate to the midplane using only the potential asymmetry originating at that end plate. Near each end, the asymmetry originating at the far end will be well symmetrized by shear and damped by the resistive drop along the line of force and will appear only as a small ripple superimposed on the asymmetry from the near end. We shall, therefore, neglect the contribution to η_l from the far end in computing the losses in each half of the machine.

In Fig. 8 we showed that in the range $I_s > 200$ A both the residual oscillations and the classical processes (resistive diffusion and end-plate recombination) contributed negligibly to the total losses. We now wish to test the hypothesis that the convective mechanism worked out in this paper is the dominant process. If this is the case, the equilibrium density n is proportional to $(dN/dt)^{-1}$ as given by Eq. (34), for constant input flux Φ. We have assumed that the density gradient does not change appreciably with shear; this has been confirmed experimentally. The error in this assumption is negligible when the asymmetry has been approximated by a pure $m = 1$ distribution.

In Fig. 19 we have plotted the peak density as a function of hard-core current I_s for two values of B_z. Points for runs at various densities have been assembled by normalizing the density to that at one value of I_s. The theoretical curves are taken from Fig. 11 and adapted to double-ended geometry by the method indicated above. It is seen that, as far as the relative increase of n with I_s is concerned, the theory fits the experiment very well if 50% of the losses are to the rod and 50% are to the outside. This ratio was checked with the radial particle collector described in Sec. IIF. The flux Φ_{out} measured by the radial collector was, indeed, about 50% of the total input flux Φ, as indicated on Fig. 19. This is not always the case, however. When one uses the Type I collimators (Sec. IID), the neutral beam is focused close to the hard core; and one finds that the shear dependence of n is consistent with $\Phi_{out}/\Phi < 10\%$. In obtaining Fig. 19, the losses to the hard core were not measured directly; these losses were checked in an auxiliary experiment. Note that the experimental points on Fig. 19 deviated from the theory only when oscillations were present in the plasma.

To compare the absolute value of the loss rate (or equilibrium density) with the convection theory, we must now specify the magnitude of η_l and the probability P that an ion will recombine on a cold surface once it reaches the loss radius a_l or b_l. In Fig. 20, the experimental n-Φ curve is compared with theory. The experimental points are obtained by extrapolating the high-shear points of Fig. 19 to zero shear, in order to remove the effect of the oscillations which exist at zero shear. The theoretical curves for convective losses are obtained from Eq. (34) by setting dN/dt equal to Φ, and Γ equal to 1, inserting the measured value of η_l, solving for $n(X)$, converting this to n_{peak} by using the measured density profile and multiplying by P. The loss radii a_l and b_l are used for X; their choice is not adjustable because it has been verified in the single-ended experiment. For loss to the hard core, the probability P must be close to 1 because once a guiding center has drifted to $r = a_l = a + r_L$, the ion will hit the hard core in one gyration. For

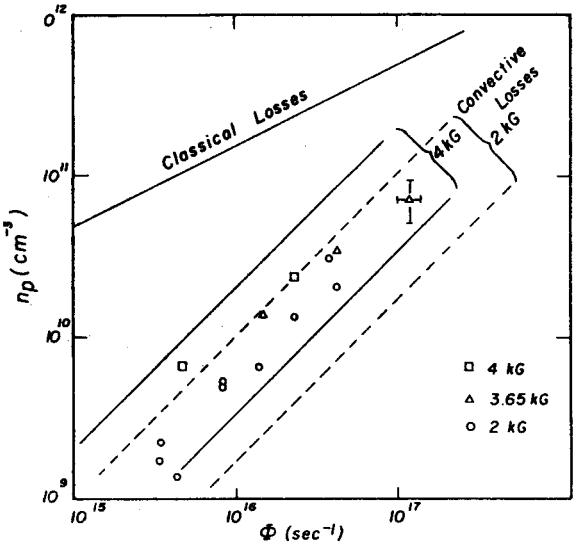

FIG. 20. Peak plasma density n_p vs input flux Φ at zero shear in double-ended operation with hard core in place. The effect of oscillations has been removed by extrapolating the curves of Fig. 19 to $I_s = 0$. The error bar shown is typical of all the points. The theoretical curve for classical losses (mainly end-plate recombination) is shown near the top. The theoretical curves for convective losses are shown, and the large spread in these predictions comes from uncertainties in applying the theory to the experiment when absolute values are involved. Compared with Fig. 1, the densities are about a factor of 2–3 lower; but a direct comparison is difficult because of differences in (a) oscillation amplitude, (b) geometry (hard core vs no hard core), (c) neutral beam collimation, and (d) end-plate temperature asymmetry.

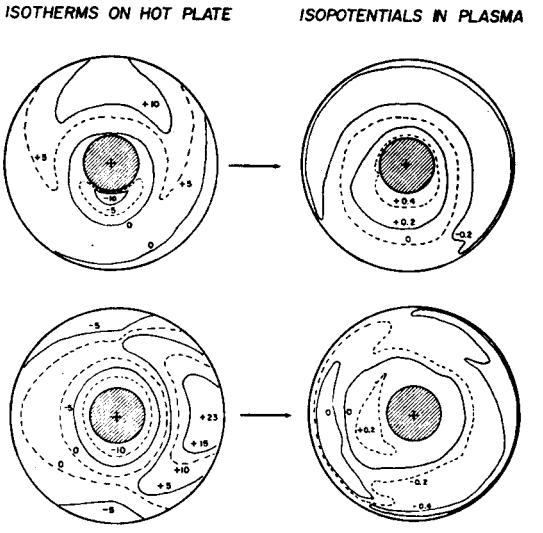

FIG. 21. Comparison of contours of temperature on the hot plate with contours of potential in the plasma. Changes in temperature are in degrees Kelvin, and changes in potential are in units of KT. In the two sets of contours the orientation of the asymmetry has been purposely changed, with all else kept constant. $B = 4$ kG, $T_c = 2500°$K.

loss to the limiters, P is difficult to determine, because there are usually large Kelvin–Helmholtz-type oscillations localized at $r = b$ which can transport ions farther out with an unknown efficiency. Since P certainly lies between 0 and 1, we have taken $P = 0.5$. Because of the uncertainties in P, in η_1, and in $n_p/n(X)$, we can only put a large band on Fig. 20 for the predicted densities. It is seen that the experimental points lie well within this band, indicating that it is possible for the convective loss mechanism to explain the entire anomalous loss in the absence of oscillations. Note that n varies linearly with Φ, as one would expect from a noncollisional process, and that the loss rate is Bohm-like, scaling roughly as $1/B$.

VI. ANCILLARY OBSERVATIONS

A. Production of Asymmetries

Up to now we have assumed that asymmetric potential distributions can arise from temperature nonuniformities in the end plates. We now show that this assumption is justified. Figure 21 shows a comparison of the temperature contours on the hot plate with the potential contours in the plasma. The former were taken with an optical pyrometer, and the latter with a floating probe only 15 cm from the hot plate to minimize diffusion and convection effects. These data were taken in single-ended operation with ions streaming unidirectionally towards a negatively biased cold plate. Hence, the ion density is given by

$$n_i = \left(\frac{j_0}{2\bar{v}_i}\right) \exp(-\eta)[1 - \operatorname{erf}(-\eta)^{1/2}] \approx \frac{j_0}{2\bar{v}_i}, \quad (38)$$

where $\eta \equiv e\phi/KT$, $\bar{v}_i \equiv (KT_i/2\pi m_i)^{1/2}$, and j_0 is the emitted ion flux. Since electrons are reflected at the cold plate, the sheath drop ϕ at the hot plate must be such as to provide the current balance

$$n_e\bar{v}_e = AT_c^2 \exp\left(-\frac{e\phi_w}{KT_c}\right) \exp\left(\frac{e\phi}{KT_c}\right), \quad (39)$$

in which T_c is the local plate temperature and the Richardson current has been written out explicitly. Setting $n_i = n_e$ and differentiating, we find

$$\nabla\eta = \nabla \ln j_0 - (2 + \eta_W - \eta)\nabla \ln T_c, \quad (40)$$

where $\eta_W = e\phi_W/KT$ is the normalized work function of tungsten, and we have assumed $T_i = T_e = T$ in the plasma. If $\partial \ln j_0/\partial\theta = 0$, $\eta \approx -5$, and $\eta_W \approx 20$, as they are in practice, the asymmetry is given by

$$\frac{\partial\eta}{\partial\theta} \approx -27\,\frac{\partial \ln T_c}{\partial\theta}. \quad (41)$$

This is nearly twice as large as the expression given in Ref. 25 for double-ended operation. Thus, a change of 10° in T_e would cause a change of about

0.1 in η (r being kept constant), and regions of high T_e would correspond to regions of low η. Both the magnitude and the direction of the asymmetry are borne out by Fig. 21. Furthermore, when the temperature asymmetry is rotated by 90° simply by changing from space-charge-limited to emission-limited operation of the hot plate bombardment system, with all else kept constant, it is seen that the potential asymmetry also rotates by 90°.

B. Density Contours

So far, we have been concerned with the effect of shear only on the potential distribution. According to Eq. (1), both n and ϕ are ideally constant along a line of force; and therefore, $n(r, \theta)$ should also exhibit a spiral structure at high shear. Figure 22 shows that this is indeed true. However, it is surprising to see that the ripples on the density profile are 180° out of phase with the potential ripples, for one normally expects high potential to be associated with high density because of the sheath relations. This phasing is independent of collisions, for it is the same at $n \approx 10^8$ as at $n \approx 10^{11}$ cm^{-3}. To understand this phase reversal, one must take into account the convective loss of ions as they stream toward the probe on the way from the hot plate to the cold plate. The probe is sufficiently far from the hot plate that most ions have made at least one revolution around the hard core by the time they reach the probe; the ions with small $v_\parallel$ will have made many revolutions. If the equipotential on which an ion is drifting crosses a loss surface, the density of ions on this equipotential will be diminished. Since this is a single-ended measurement, ions crossing the outer loss radius b_1 will not be lost, for they will drift back in (if the equipotentials are closed) and strike the probe before striking the end plate. However, ions crossing the inner loss radius a_1 will strike the hard core before reaching the probe. Looking at Fig. 22, one sees that the symmetric part of the potential—averaged over the ripples—is peaked near the hard core. When the potential distribution is shifted by the temperature nonuniformity of the end plate, the drift surfaces with high potential will be shifted even nearer to the hard core and, hence, will suffer from convective losses more than other drift surfaces. This is the reason that, as far as the asymmetric part is concerned, the density is low where the potential is high, and vice versa. Once the value of αz is large enough for the convective losses to be greatly diminished, this relation between n and ϕ is frozen; and for larger z one simply has n and ϕ constant along a line of force. Since only losses to the hard core in a length Δz of $\sim$160 cm are involved, this is a relatively small effect. Indeed, Fig. 22 shows that the density ripple amplitude is only $\sim$5%, whereas the potential ripple amplitude is $\sim$25% of KT.

Note that an alternative explanation turns out to have the wrong sign. Although n and ϕ are in phase as far as the symmetric part of the distribution, due to $j_0(r)$, is concerned, they might be expected to be out of phase as far as the asymmetric part, due to ∇T_e, is concerned, because high ϕ is associated with low T_e. However, the ionization probability of a neutral atom on the hot plate does not decrease as T_e is lowered; it increases because the Saha equation is of the form $n_i/n_n \propto \exp[e(\phi_W - \phi_I)/KT]$, where ϕ_I is the ionization potential and is less than ϕ_W.

Figure 23 illustrates further the change in density distribution due to convective losses. At $z = 15$ cm, the potential has an $m = 1$ asymmetry due to ∇T_e, but the ion density is determined mainly by $j_0(r)$ and is quite symmetric. At $z = 76$ cm, the potential contours retain their general shape, but the density contours have been greatly distorted. Looking closely at the curves, one will see that the density on equipotentials passing close to the hard core has been greatly decreased, while the density on equipotentials far from the hard core has decreased only slightly.

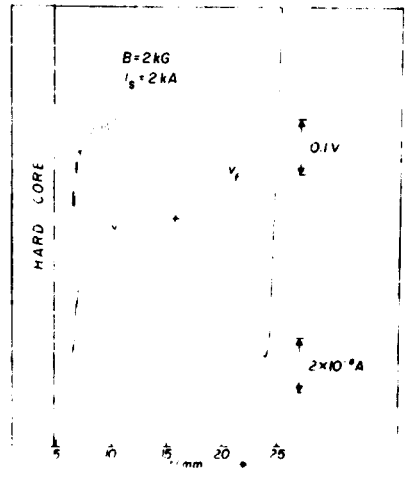

FIG. 22. [illegible] recorder traces of [illegible] potential profiles [illegible] single-ended [illegible] high [illegible]. The [illegible] about 160 cm away [illegible] the hot plate.

C. Damping of Potential Ripples

If potential were truly constant along a line of force, the amplitude of the ripples in the radial potential profile would be constant, as shown by Eq. (5). Figure 13 shows, however, that the ampli-

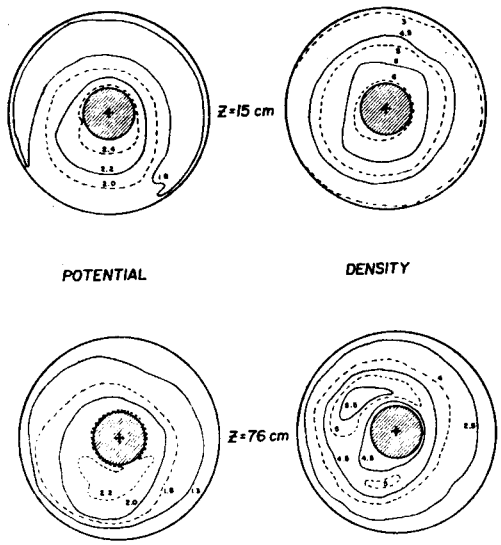

FIG. 23. Development of potential and density profiles in single-ended operation as the plasma streams along the axis in the absence of shear. The potential contours are labeled in units of $e\phi/kT$, and the density contours in units proportional to the ion saturation current.

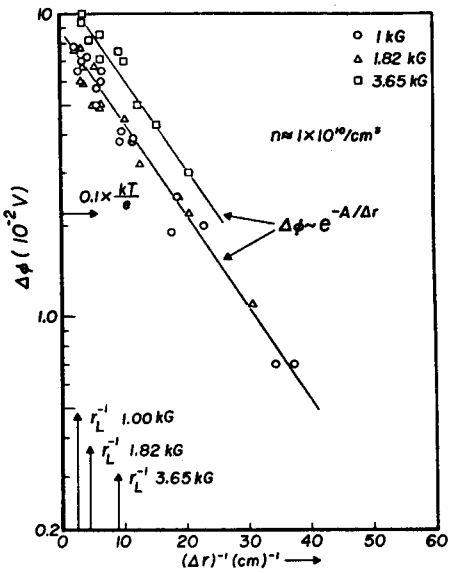

FIG. 24. Peak-to-peak amplitude of potential ripples vs reciprocal of ripple spacing Δr. The various points at a given magnetic field are obtained by varying the shear or the radius.

tude actually decreases with the ripple spacing Δr. A plot of the ripple amplitude $\Delta\phi$ vs $(\Delta r)^{-1}$ is given in Fig. 24. $\Delta\phi$ is found to follow the relation

$$\Delta\phi \propto \exp\left(-\frac{A}{\Delta r}\right), \tag{42}$$

where A is a constant. We believe that the fine-scaled ripples are damped by collisions. Ion–electron collisions would affect only scale lengths of the order of the electron Larmor radius, but ion–ion collisions could provide a cross-field mobility which short circuits potential variations on the scale of r_{Li}. To estimate this effect, we consider that the ions undergo a random walk with a step length $\approx a_i$. The number of steps, or collisions, experienced by an ion in traveling a distance z from the hot plate is approximately z/λ_{ii}. The random-walk excursion $(\Delta x)_{\text{rms}}$ is then given by $(\Delta x)_{\text{rms}} \approx a_i(z/\lambda_{ii})^{1/2}$. When this becomes comparable to Δr, the potential variations will be shorted out, so one would expect a law of the form

$$\Delta\phi \propto \exp\left(-\frac{a_i(z/\lambda_{ii})^{1/2}}{\Delta r}\right). \tag{43}$$

To test this formula, which agrees with Eq. (42), we studied the density dependence of the coefficient $A = a_i(z/\lambda_{ii})^{1/2} \propto n^{1/2}$. In Fig. 25 we plot $\Delta\phi$ vs $(\Delta r)^{-1}$ for various densities at constant magnetic field. In Fig. 26, the slopes of these curves are used to give a plot of A vs n. We see that the $n^{1/2}$ dependence of A is obeyed. However, the B dependence predicted by Eq. (43) is not found in Fig. 24. We have not been able to explain this, and it remains a loose thread in our analysis.

The comparison between theory and experiment made in Sec. V was made neglecting this change in $\Delta\phi$ with Δr. We now show that this omission is justified. The important point here is that the

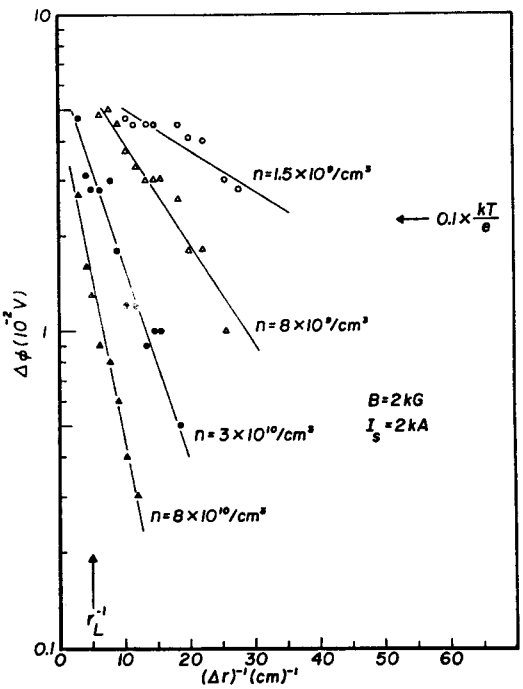

FIG. 25. Ripple amplitude vs $(\Delta r)^{-1}$ for various densities.

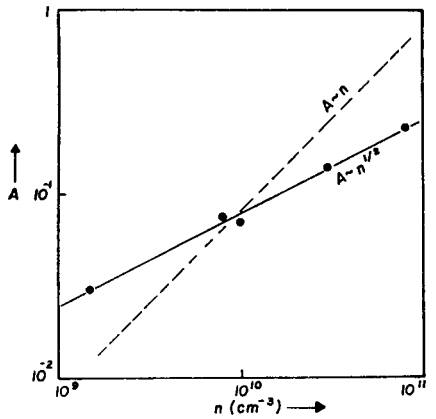

FIG. 26. The slope A of the curves of Figs. 24 and 25 as a function of density n.

convective losses occur mainly in the region near the ends of the machine, where the convective patterns have not been tightly twisted into spirals. In the region near the midplane, the drift paths have been symmetrized by shear, and very little loss occurs there. The transition occurs at a position z where $\Delta r \approx a_i$. Since $\Delta\phi$ is significantly decreased only for $\Delta r \leq a_i$, the change in $\Delta\phi$ affects only the region near the midplane, where the radial losses are small anyway.

To do this quantitatively, we note that in the evaluation of the loss rate $\dot{N}$ [Eq. (33)], the effect of a varying $\Delta\phi$ would make $\bar{v}_x$ vary with z in a different manner. In the expression Eq. (30) for $\bar{v}_x$, we see that the effect of ripple damping can be included merely by allowing $\eta_1(x)$ to also be a function of z. According to Eq. (43), we take

$$\eta_1 \propto \exp(-a\zeta),$$

where $\zeta \equiv \pi a_i/2^{1/2}\,\Delta r$. The exponential in Eq. (30) or Eq. (32) can also be expressed in terms of ζ with the use of Eq. (10):

$$\exp\left[-\frac{1}{2}\left(\frac{\alpha z a_i}{r^3}\right)^2\right] = \exp(-\zeta^2).$$

Redoing the z integration in Eq. (33), we find that the ratio of loss rate including collisional effects is decreased by the factor

$$\frac{\dot{N}_c}{\dot{N}} = \int_0^{\zeta_{\max}} \exp(-\zeta^2 - \zeta a)\,d\zeta \Big/ \int_0^{\zeta_{\max}} \exp(-\zeta^2)\,d\zeta$$
$$= \frac{\exp(a^2/4)[\operatorname{erf}(\zeta_{\max} + \frac{1}{2}a) - \operatorname{erf}(\frac{1}{2}a)]}{\operatorname{erf}\zeta_{\max}},$$

where $\zeta_{\max}$ is the value of ζ at the midplane. For high shear ($\zeta_{\max} \gg 1$), we have

$$\frac{\dot{N}_c}{\dot{N}} \approx \exp\left(\frac{a^2}{4}\right)\left[1 - \operatorname{erf}\left(\frac{a}{2}\right)\right]. \qquad (44)$$

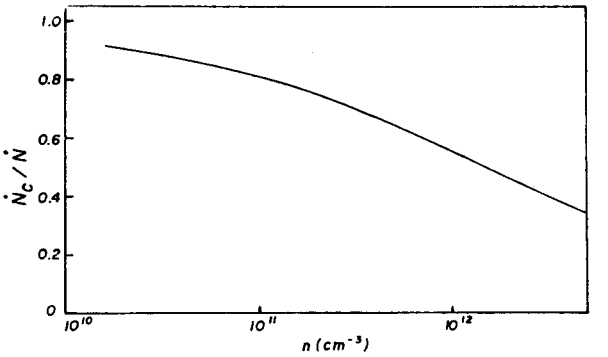

FIG. 27. The effect of ion–ion collisions on the computed convective loss rate as a function of density.

This relation is shown in Fig. 27, with the n dependence of the coefficient a taken from the data of Fig. 25. It is seen that for the densities of $< 10^{11}$ cm^{-3} used in this experiment, the correction due to variation of $\Delta\phi$ is less than 20%.

D. Measurement of Inward Losses

In most of this work the flux to the hard core was inferred from the input flux and the measured flux to the outside. In a separate run, we inserted internal limiters and plasma eaters (see Fig. 6M) to try to measure the inward loss directly. There were two inner limiters 1.9 cm in diameter, each placed about 10 cm from a hot plate. Each limiter consisted of two metal rings. The ring facing the hot plate was floating and served to shield the other ring from the hot plate. The rings facing the midplane, 3 m apart, were then biased like a double probe. Since the limiter radius was only 0.48 cm larger than the hard-core radius, the scrape-off layer was only about 2 Larmor radii thick; consequently, some of the inward flux was lost to the hard core without being measured on the collectors. The outer flux collector was described in Sec. IIF. According to the theory presented there, the currents to both collectors was doubled to give the fluxes Φ_o and Φ_i to the outside and the inside, respectively. Both sets of collectors gave current–voltage characteristics with rather good saturation. The currents were found by extrapolating to zero voltage, and the error in this extrapolation was less than 5%.

Figure 28 shows the total radial flux $\Phi_o + \Phi_i$ and the ratio Φ_o/Φ_i as a function of I_s. At low shear, the total radial flux was somewhat less than the input flux because some ions were lost to the hard core, and some escaped beyond the outer radius of the outer collector. The discrepancy was not due to recombination, which was negligible. At higher shear, all of the input flux shows up on the radial

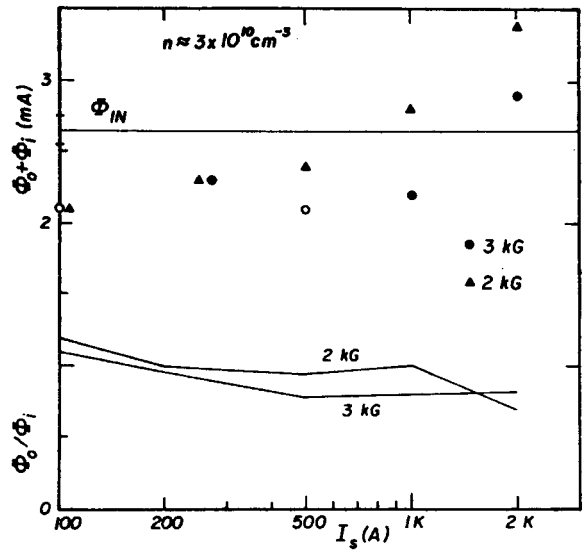

FIG. 28. Measured radial ion fluxes to the outside (Φ_o) and to the inside (Φ_i) vs shear in double-ended operation. The points show the sum $\Phi_o + \Phi_i$ as compared with the measured total input flux Φ_{IN}. The lines show the ratio Φ_o/Φ_i. The plasma was quiescent except for the open points, when oscillations of 15% amplitude were present.

collectors. The fact that $\Phi_o + \Phi_i$ exceeds Φ_{IN} at $I_s = 2$ kA is probably due to an increase in Φ_{IN} arising from the evaporation of neutral potassium from the hard core when it warms up. The ratio Φ_o/Φ_i at zero shear is approximately 1. This confirms the assumption made in Sec. V, where it was shown that theory and experiment agreed if the inside and outside losses were about equal.

VII. CONCLUSIONS

Our results may be summarized as follows:

(1) At low densities in a double-ended Q machine there is an anomalous loss process of magnitude $\geq$ Bohm diffusion, and the loss persists when oscillations are absent.

(2) Small temperature irregularities on the end plates are shown experimentally to give rise to asymmetric electric fields in the plasma. The resulting convective drifts are large enough to explain the losses.

(3) Magnetic shear is shown experimentally to reduce the anomalous losses dramatically. The improvement in confinement is much larger than can be explained by suppression of oscillations, by a decrease in recombination, by an increase in total magnetic field strength, or by the creation of a magnetic well.

(4) A mechanism is described by which shear can reduce plasma convection. A detailed theory is given to predict the increase of confinement with shear.

(5) The predictions of the theory are verified experimentally in both single-ended and double-ended geometry. The amount of twisting of equipotentials is verified to better than 10%. The increase in confinement with shear agrees with theory to within ~30%. The effect of collisions is shown to alter these results by less than 20%.

We wish to point out that the possibility of adding shear was essential to proving that convection is the cause of nonoscillatory losses in Q machines. Although one can easily estimate that $\mathbf{E} \times \mathbf{B}$ drifts can bring ions to the vicinity of the radial boundary with sufficient rapidity, it is difficult to know if the ions will actually be lost there. A complicated situation exists at the limiter radius: equipotentials tend to be parallel to $\hat{\theta}$ there, a large radial potential barrier exists to prevent ions from going out, and there is the question of finite transit time along $\mathbf{B}$ to the limiter. The observed dependence of the losses with shear, however, leaves little doubt that convection is the loss mechanism. For instance, this dependence rules out the possibility that the losses are due to enhanced end-plate recombination or to simple scrape off of ions with large Larmor radii.

Our picture of the loss mechanism would predict that losses would decrease if the equipotential contours were made more symmetric. This has been verified recently by Guilino,[38] who symmetrized the end-plate temperature distribution by rotating the heating filaments, and by Jassby and Motley,[39] who circularized the drift surfaces by deliberately introducing a large radial gradient.

There still remains a question of what would happen in the limit of very small Larmor radii or very low collision frequency. In our experiment we had to work in the regime in which an ion could easily jump from a "confined" equipotential to an "unconfined" equipotential by making one or two collisions. At higher magnetic fields and temperatures, the loss rate should eventually be limited not by the convection velocity but by the diffusion from confined to unconfined drift surfaces. The mechanism would then be similar to that described by Galeev *et al.*[40] for enhanced collisional diffusion.

Finally, we wish to emphasize that dc convection is *not* the sole cause of anomalous losses in a Q machine. As shown clearly in Fig. 8, oscillations also cause anomalous losses; but these are outside the scope of this paper.

ACKNOWLEDGMENTS

It is a pleasure to acknowledge the help of Professor K. C. Rogers, who participated in all phases

of the experiment. We thank Professor R. M. Kulsrud and Professor T. H. Stix for critical readings of the theory. Mr. K. P. Mann ably directed the operation of the machine, and Mr. W. L. Lamont skillfully fabricated the probes and hot-plate assemblies. In the hot-probe work which initially convinced us of the reality of this effect, we were aided by R. Chang.

This work was performed under the auspices of the United States Atomic Energy Commission, Contract AT(30-1)-1238.

APPENDIX

With the expansion (29), the components of Eq. (24) become

$$\frac{dv_x}{d\tau}+\epsilon\frac{dv_x}{d\tau_1}+\epsilon^2\frac{dv_x}{d\tau_2}+\cdots-v_y = -\frac{a_i\eta_0'}{\epsilon}-\frac{a_i\eta^{(1)\prime}}{\epsilon}-\frac{\gamma v_z}{\epsilon},$$

$$\frac{dv_y}{d\tau}+\epsilon\frac{dv_y}{d\tau_1}+\epsilon^2\frac{dv_y}{d\tau_2}+\cdots+v_x=\frac{a_i}{\epsilon^2}\frac{\partial\eta^{(1)}}{\partial y}, \tag{A1}$$

$$\frac{dv_z}{d\tau}+\epsilon\frac{dv_z}{d\tau_1}+\epsilon^2\frac{dv_z}{d\tau_2}+\cdots-\frac{\gamma v_z}{\epsilon}=\frac{a_i}{\epsilon^3}\frac{\partial\eta^{(1)}}{\partial z},$$

where $' = \partial/\partial x$ and $\mathbf{v} \equiv \mathbf{v}/v_s$. The ordering given by Eqs. (27) and (28) has been shown. To lowest order, we have

$$\frac{dv_x^{(0)}}{d\tau}=v_y^{(0)},\qquad \frac{dv_y^{(0)}}{d\tau}=-v_x^{(0)},$$
$$\frac{dv_z^{(0)}}{d\tau}=0,\qquad \frac{d\mathbf{x}^{(0)}}{d\tau}=a_i\mathbf{v}^{(0)}. \tag{A2}$$

This describes the cyclotron motion:

$$\begin{aligned} v_x^{(0)} &= v_\perp\cos(\tau+\Phi),\\ v_y^{(0)} &= -v_\perp\sin(\tau+\Phi), \qquad\qquad (A3)\\ v_z^{(0)} &= v_{z0},\\ x^{(0)} &= x_0+a_iv_\perp\sin(\tau+\Phi),\\ y^{(0)} &= y_0+a_iv_\perp\cos(\tau+\Phi), \qquad\qquad (A4)\\ z^{(0)} &= z_0+v_{z0}\tau, \end{aligned}$$

where $v_\perp$, Φ, v_{z0}, x_0, y_0, and z_0 are constant on the τ time scale but may vary on the slower $\tau_1, \tau_2, \cdots$ time scales.

In first order, Eqs. (A1) become

$$\frac{dv_x^{(1)}}{d\tau}+\epsilon\frac{dv_x^{(0)}}{d\tau_1}-v_y^{(1)}=-a_i\frac{\partial\eta}{\partial x}-\gamma v_z^{(0)},$$
$$\frac{dv_y^{(1)}}{d\tau}+\epsilon\frac{dv_y^{(0)}}{d\tau_1}+v_x^{(1)}=0,$$
$$\frac{dv_z^{(1)}}{d\tau}+\epsilon\frac{dv_z^{(0)}}{d\tau_1}=\gamma v_z^{(0)}, \tag{A5}$$
$$a_i\mathbf{v}^{(1)}=\frac{d\mathbf{x}^{(1)}}{d\tau}+\epsilon\frac{d\mathbf{x}^{(0)}}{d\tau_1},$$

in which γ and $\partial\eta/\partial x$ are to be evaluated at $\mathbf{x} = \mathbf{x}^{(0)}$. To obtain the guiding center motion, we average over a cyclotron period to remove the gyratory motion. If

$$\langle\xi\rangle \equiv (2\pi)^{-1}\int_{-\pi}^{\pi}\xi\,d\tau,$$

we have

$$\left\langle\frac{d\xi}{d\tau}\right\rangle=0,\quad a_i\langle\mathbf{v}^{(1)}\rangle=\epsilon\frac{d\mathbf{x}_0}{d\tau_1},\quad \left\langle\frac{dv_{x,y}^{(0)}}{d\tau_1}\right\rangle=0. \tag{A6}$$

Expanding $\gamma(x^{(0)})$ about $x^{(0)} = x_0$ and keeping only the lowest term, we then find

$$\langle v_x^{(1)}\rangle=0,\qquad \epsilon\frac{dv_{x0}}{d\tau_1}=0,$$
$$\langle v_y^{(1)}\rangle=\gamma(x_0)v_{x0}+a_i\langle\eta'(\mathbf{x}^{(0)})\rangle. \tag{A7}$$

Thus, there is no radial drift to this order, and the azimuthal drift is simply the sum of the E_r/B drift (averaged over a Larmor orbit) and the rotation due to motion along a helical line of force.

In second order, the last two of Eqs. (A1) give

$$\frac{dv_y^{(2)}}{d\tau}+\epsilon\frac{dv_y^{(1)}}{d\tau_1}+\epsilon^2\frac{dv_y^{(0)}}{d\tau_2}+v_x^{(2)}=-a_i\left[\frac{\partial\eta}{\partial y}\right]_{\mathbf{x}=\mathbf{x}^{(0)}},$$
$$\frac{dv_z^{(2)}}{d\tau}+\epsilon\frac{dv_z^{(1)}}{d\tau_1}+\epsilon^2\frac{dv_z^{(0)}}{d\tau_2} = \gamma(x_0)v_x^{(1)}+a_iv_\perp\gamma'(x_0)\sin(\tau+\Phi)v_z^{(0)}. \tag{A8}$$

The term $\epsilon dv_y^{(1)}/d\tau_1$, when averaged over τ, can be shown to be actually of $O(\epsilon^3)$. Since $\langle v_y^{(1)}\rangle$ is a function of the zero-order guiding center position $\mathbf{x}_0$, this term can be written

$$\epsilon\frac{d}{d\tau_1}\langle v_y^{(1)}\rangle=\epsilon\frac{dx_0}{d\tau_1}\frac{\partial}{\partial x_0}\langle v_y^{(1)}\rangle+\epsilon\frac{dy_0}{d\tau_1}\frac{\partial}{\partial y_0}\langle v_y^{(1)}\rangle+\epsilon\frac{dz_0}{d\tau_1}\frac{\partial}{\partial z_0}\langle v_y^{(1)}\rangle.$$

With the help of the middle of Eqs. (A6), this becomes

$$\epsilon\frac{d}{d\tau_1}\langle v_y^{(1)}\rangle=a_i\left[\langle v_x^{(1)}\rangle\frac{\partial}{\partial x_0}+\langle v_y^{(1)}\rangle\frac{\partial}{\partial y_0}+\langle v_z^{(1)}\rangle\frac{\partial}{\partial z_0}\right]\langle v_y^{(1)}\rangle=O(\epsilon^3).$$

The first term in [ ] vanishes because $\langle v_x^{(1)} \rangle = 0$, and the other terms are of $O(\epsilon^3)$ because the gradients in the y and z directions are small; it is only $a_i\, \partial/\partial x$ which can be of $O(1)$. With this simplification, the short-time average of Eqs. (A8) gives

$$\langle v_x^{(2)} \rangle = -a_i \left\langle \frac{\partial \eta^{(1)}(\mathbf{x}^{(0)})}{\partial y} \right\rangle, \qquad \epsilon \frac{d}{d\tau_1} \langle v_z^{(1)} \rangle = -\epsilon^2 \frac{d}{d\tau_2} v_{z0} = 0. \tag{A9}$$

The last equality is a consequence of the condition that $\langle v_z^{(1)} \rangle$ must not be allowed to blow up on the τ_1 time scale; one integrates the last line with respect to τ_1 using Eq. (A7) to show that v_{z0} is constant on the τ_1 scale. Thus, the loss term v_x first appears in second order, but we must go to higher order to find $\langle v_z^{(1)} \rangle$.

In third order, we have

$$\begin{aligned} \frac{d}{d\tau} v_z^{(3)} + \epsilon \frac{d}{d\tau_1} v_z^{(2)} + \epsilon^2 \frac{d}{d\tau_2} v_z^{(1)} + \epsilon^3 \frac{d}{d\tau_3} v_z^{(0)} &= -a_i \left[\frac{\partial \eta}{\partial z} \right]_{\mathbf{x}=\mathbf{x}^{(0)}} \\ &\quad + \gamma(x_0) v_x^{(2)} + a_i v_\perp \sin(\tau + \Phi) \gamma'(x_0) v_x^{(1)} \\ &\quad + \tfrac{1}{2}[a_i v_\perp \sin(\tau + \Phi)]^2 \gamma''(x_0) v_x^{(0)}. \end{aligned}$$

Taking the short-time average, we find

$$\epsilon^2 \frac{d}{d\tau_2} \langle v_z^{(1)} \rangle + \epsilon^3 \frac{d}{d\tau_3} v_{z0} = -a_i \left\langle \frac{\partial \eta(\mathbf{x}^{(0)})}{\partial z} \right\rangle + \gamma(x_0) \langle v_x^{(2)} \rangle. \tag{A10}$$

The extremely slow variation of $\langle v_z \rangle$ is due to the fact that the driving term $a_i\, \partial\eta/\partial z$ was taken to be of $O(\epsilon^3)$.

To evaluate $\eta^{(1)}(\mathbf{x})$ it is convenient to transform to a coordinate system complying with the lines of force:

$$x' = x, \qquad y' = y - \gamma(x) z, \qquad z' = z,$$
$$\frac{\partial \eta}{\partial x} = \frac{\partial \eta}{\partial x'} - \gamma'(x')\, z' \frac{\partial \eta}{\partial y'}, \tag{A11}$$
$$\frac{\partial \eta}{\partial y} = \frac{\partial \eta}{\partial y'}, \qquad \frac{\partial \eta}{\partial z} = \frac{\partial \eta}{\partial z'} - \gamma(x') \frac{\partial \eta}{\partial y'},$$

where $\gamma'(x') \equiv d\gamma/dx'$. The potential η now varies slowly in x'; the rapid x variation across the ripples of the spiral pattern is contained in the large coefficient $\gamma' z'$.

We next expand η in a Taylor series about $\mathbf{x}_0$

$$\eta(\mathbf{x}^{(0)}) = \eta_0(x_0') + \sum_{j=0}^{\infty} (-1)^j \frac{\beta^j}{j!} v_\perp^j \cdot \sin^j(\tau + \Phi) \frac{\partial^j}{\partial y'^j} \eta^{(1)}(\mathbf{x}_0') + O(\epsilon), \tag{A12}$$

where we have used Eqs. (A4) and (A11), and

$$\beta \equiv a_i \gamma'(x_0') z_0' = a_i \gamma'(x_0) z_0 = O(1). \tag{A13}$$

Upon substituting Eq. (A12) into Eqs. (A7), (A9), and (A10) and taking the average over τ, the odd terms in the sum disappear, and the result can be written

$$\langle v_y^{(1)} \rangle = \gamma(x') v_z^{(0)}(x') + a_i \frac{\partial \eta_0}{\partial x'} - \beta \frac{\partial \chi}{\partial y'}, \qquad \langle v_x^{(2)} \rangle = -a_i \frac{\partial \chi}{\partial y'}, \qquad \epsilon^2 \frac{d}{d\tau_2} \langle v_z^{(1)} \rangle + \epsilon^3 \frac{d}{d\tau_3} v_z^{(0)} = -a_i \frac{\partial \chi}{\partial z'}, \tag{A14}$$

where

$$\chi \equiv \sum_{i=0}^{\infty} \left(\frac{\beta}{2}\right)^{2i} \frac{v_\perp^{2i}}{(j!)^2} \frac{\partial^{2i}}{\partial y'^{2i}} \eta^{(1)}(\mathbf{x}') = O(\epsilon). \tag{A15}$$

We have dropped the subscript zero; it is understood that the variables refer to the ion guiding center. Note that v_x, v_y, and v_z are taken along (x, y, z), and not (x', y', z'). Note also that we have neglected $\partial/\partial x'$ relative to $\gamma' z' \partial/\partial y'$. The approximation breaks down at small $\gamma' z'$, but the $\partial/\partial x'$ term gives only a small and harmless azimuthal drift in any case.

When $\beta = 0$ (no shear), χ reduces to $\eta^{(1)}$, and Eq. (A14) merely gives the $\mathbf{E} \times \mathbf{B}$ drifts in the zero-Larmor-radius limit. When β is small but finite, Eq. (A15) gives

$$\chi \approx \eta^{(1)} + \left(\frac{\beta}{2}\right)^2 v_\perp^2 \frac{\partial^2 \eta^{(1)}}{\partial y'^2} \approx \eta^{(1)} + \tfrac{1}{2} a_s^2 v_\perp^2 \frac{\partial^2 \eta^{(1)}}{\partial x^2}, \tag{A16}$$

which is the usual finite-Larmor-radius correction. Note, however, that the finite-Larmor-radius corrections in $\partial \eta^{(1)}/\partial y$ and $d\eta_0/dx$ are higher-order in ϵ and have been neglected. The only short scale lengths in our geometry come from the tight spirals caused by shear.

Finally, we must integrate over a velocity distribution in order to get an expression for the motion of the fluid of guiding centers. Equation (A14) gives the motion of a guiding center at a point in space. We average over all particles with guiding centers at the same point but with different values

of a_i. Note that this does not give a fluid velocity but an average guiding center velocity. It will be sufficient to choose a Maxwellian distribution $f_M(\mathbf{v})$, with possibly a shift $\bar{v}_z^{(0)}$ along the z axis. Defining

$$\bar{v} \equiv \int f_M(\langle \mathbf{v} \rangle)\, d\mathbf{v}, \qquad \bar{\chi} \equiv \sum_{j=0}^{\infty} \left(\frac{\beta}{2}\right)^{2j} \frac{1}{j!} \frac{\partial^{2j}\eta^{(1)}}{\partial y'^{2j}}, \tag{A17}$$

and averaging Eq. (A14) over velocities, we obtain

$$\bar{v}_y^{(1)} = \gamma(x')\bar{v}_z^{(0)} + a_i \frac{\partial \eta_0}{dx'} - \beta \frac{\partial \bar{\chi}}{\partial y'},$$

$$\bar{v}_x^{(2)} = -a_i \frac{\partial \bar{\chi}}{\partial y'}, \tag{A18}$$

$$-a_i \frac{\partial \bar{\chi}}{\partial y'} \frac{d\bar{v}_z^{(0)}}{dx'} + a_i \frac{d\eta_0}{dx'} \frac{\partial \bar{v}_z^{(1)}}{\partial y'} + \bar{v}_z^{(0)} \frac{\partial \bar{v}_z^{(1)}}{\partial z'} = -\frac{\partial \bar{\chi}}{\partial z'}.$$

In the last equation, we have replaced the time derivatives with the appropriate convective derivatives.

So far, the potential distribution $\eta_0(x) + \eta^{(1)}(\mathbf{x})$ has been arbitrary. To make further progress, we must now take a specific form for $\eta^{(1)}$:

$$\eta^{(1)} = \eta_1(x') \sin ky'. \tag{A19}$$

Using this in Eq. (A18), we finally obtain

$$\bar{v}_y^{(1)} = \gamma(x')\bar{v}_z^{(0)} + a_i \frac{d\eta_0}{dx'} - k\beta\eta_1(x') \cdot \cos ky' \exp(-\tfrac{1}{2}k^2\beta^2), \tag{A20}$$

$$\bar{v}_x^{(2)} = -ka_i\eta_1(x') \cos ky' \exp(-\tfrac{1}{2}k^2\beta^2).$$

The last line is the same as Eq. (30).

One might have thought that this result could have been obtained from the theory of waves in a hot plasma[41] by setting $\omega = 0$. However, it is not easy to adapt the theory for our purposes because k_x, k_y, and k_z are interconnected in a particular way by the shear. We have preferred to derive the result from scratch with an ordering appropriate to the experiment. An advantage of this is that the z dependence is explicitly obtained.

* Based on doctoral dissertation. Present address: Los Alamos Scientific Laboratory, Los Alamos, New Mexico.

[1] N. Rynn, Rev. Sci. Instr. **35**, 40 (1964).

[2] F. F. Chen, J. Nucl. Energy, Pt. C **7**, 399 (1965).

[3] H. W. Hendel, B. Coppi, F. Perkins, and P. A. Politzer, Phys. Rev. Letters **18**, 438 (1967).

[4] F. F. Chen, D. Mosher, and K. C. Rogers, in *Plasma Physics and Controlled Nuclear Fusion Research* (International Atomic Energy Agency, Vienna, 1969), Vol. I, p. 625.

[5] F. F. Chen, Phys. Fluids **9**, 965 (1966). A large number of other authors have also treated the question of shear stabilization.

[6] N. D'Angelo and N. Rynn, Phys. Fluids **4**, 1303 (1961); N. Rynn, *ibid.* **7**, 1084 (1964).

[7] S. von Goeler, Phys. Fluids **7**, 463 (1964).

[8] T. K. Chu, H. W. Hendel, R. W. Motley, F. Perkins, P. A. Politzer, T. H. Stix, and S. von Goeler, in *Plasma Physics and Controlled Nuclear Fusion Research* (International Atomic Energy Agency, Vienna, 1969), Vol. I, p. 611.

[9] M. Hashmi, A. J. van der Houven van Oordt, and J.-G. Wegrowe, in *Plasma Physics and Controlled Nuclear Fusion Research* (International Atomic Energy Agency, Vienna, 1969), Vol. I, p. 675.

[10] N. D'Angelo, Phys. Fluids **7**, 1086 (1964).

[11] R. W. Motley, Phys. Fluids **8**, 205 (1965).

[12] L. Spitzer, Jr., Phys. Fluids **3**, 659 (1960).

[13] S. von Goeler and R. W. Motley, in *Proceedings of Conference on Physics of Quiescent Plasmas* (Euratom-CNEN, Frascati, Italy, 1967), Pt. I, p. 243; also Phys. Fluids **10**, 1360 (1967).

[14] N. D'Angelo and S. von Goeler, Nucl. Fusion **5**, 279 (1965).

[15] M. Hashmi, A. J. van der Houven van Oordt, and J.-G. Wegrowe, Plasma Phys. **10**, 861 (1968).

[16] N. S. Buchel'nikova, Nucl. Fusion **6**, 122 (1966).

[17] N. S. Wolf and K. C. Rogers, Phys. Fluids **9**, 2294 (1966).

[18] J. A. Decker, P. J. Freyheit, W. D. McBee, and L. T. Shepherd, Phys. Fluids **10**, 2442 (1967).

[19] B. J. Eastlund and C. K. Chu, Phys. Fluids **9**, 161 (1966).

[20] B. J. Eastlund, Phys. Fluids **9**, 594 (1966).

[21] K. Josephy, B. J. Eastlund, and T. C. Marshall, Phys. Fluids **10**, 1112 (1967).

[22] H. W. Hendel, T. K. Chu, and P. A. Politzer, Phys. Fluids **11**, 2426 (1968).

[23] F. F. Chen and D. Mosher, Phys. Rev. Letters **18**, 639 (1967).

[24] Note that only the transport of ions is under scrutiny in Q machines operating under so-called electron-sheath conditions. The end plates supply electrons as needed for charge neutrality, and the transport does not have to be ambipolar.

[25] F. F. Chen, Phys. Fluids **9**, 2534 (1966). The danger of temperature gradients in the end plates has also been pointed out independently by L. T. Shepherd, G. Grieger, and C. W. Hartman.

[26] C. W. Hartman and R. H. Munger, in *Proceedings of Conference on Physics of Quiescent Plasmas* (Euratom-CNEN, Frascati, Italy, 1967), Pt. I, p. 49.

[27] D. Bohm, E. H. S. Burhop, H. S. W. Massey, and R. M. Williams, in *Characteristics of Electrical Discharges in Magnetic Fields*, A. Guthrie and R. K. Wakerling, Eds. (McGraw-Hill Book Company, New York, 1949), Chap. 9.

[28] R. A. Dory, D. W. Kerst, D. M. Meade, W. E. Wilson, and C. W. Erickson, Phys. Fluids **9**, 997 (1966).

[29] W. L. Harries, Phys. Fluids **13**, 140 (1970).

[30] F. F. Chen, Rev. Sci. Instr. **40**, 1049 (1969).

[31] F. F. Chen, C. Etievant, and D. Mosher, Phys. Fluids **11**, 811 (1968).

[32] F. F. Chen, in *Proceedings of Conference on Physics of Quiescent Plasmas* (Euratom-CNEN, Frascati, Italy, 1967), Pt. II, p. 563.

[33] F. F. Chen, Physics Today, October **20**, 115 (1967).

[34] R. W. Motley and D. L. Jassby, Phys. Rev. Letters **22**, 333 (1969).

[35] H. Dreicer and D. B. Henderson, Phys. Rev. Letters **20**, 374 (1968).

[36] We are indebted to J. D. Jukes for the germ of this idea.

[37] G. Schmidt, *Physics of High Temperature Plasmas* (Academic Press Inc., New York, 1966), p. 292.

[38] E. Guilino, P. Müller, K. Sahner, and K. Trambauer, in *Proceedings of the International Conference on Physics of Quiescent Plasmas* (Ecole Polytechnique, Paris, 1969), Vol. 2, p. 108; E. Guilino and N. Troppmann, *ibid.*, p. 117; Phys. Fluids (to be published).

[39] D. L. Jassby and R. W. Motley, Phys. Fluids **12**, 258 (1969).

[40] A. A. Galeev, R. Z. Sagdeev, H. P. Furth, and M. N. Rosenbluth, Phys. Rev. Letters **22**, 511 (1969).

[41] T. H. Stix, *The Theory of Plasma Waves* (McGraw-Hill Book Company, New York, 1962), Chap. 8.